Published in final edited form as:

Neuroimage. 2018 November 15; 182: 39–61. doi:10.1016/j.neuroimage.2018.06.046.

Physical and Numerical Phantoms for the validation of brain microstructural MRI: A Cookbook

Els Fieremans[*] and **Hong-Hsi Lee**

Center for Biomedical Imaging, Department of Radiology, New York University School of Medicine, New York, NY, USA

[*]Corresponding author, Address all correspondence to: Els Fieremans, Department of Radiology, NYU Langone Medical Center, 660 First Avenue, 2nd floor, New York, NY 10016, Els.Fieremans@nyumc.org, Tel.: (212) 263-3344; Fax: (212) 263-4830.

Figure 1 is adapted with permission from (1) Wang, X., Reeder, S. B. and Hernando, D. (2017), An acetone-based phantom for quantitative diffusion MRI. Journal of Magnetic Resonance Imaging, 46: 1683–1692. doi:10.1002/jmri.25727 Copyright 2017 Wiley; (2) Fieremans, E., Pires, A. and Jensen, J. H. (2012), A simple isotropic phantom for diffusional kurtosis imaging. Magnetic Resonance in Medicine, 68: 537–542. doi:10.1002/mrm.23263 Copyright 2012 Wiley; (3) Nilsson, M., Larsson, J., Lundberg, D., Szczepankiewicz, F., Witzel, T., Westin, C., Bryskhe, K. and Topgaard, D. (2018), Liquid crystal phantom for validation of microscopic diffusion anisotropy measurements on clinical MRI systems. Magnetic Resonance in Medicine, 79: 1817–1828. doi: 10.1002/mrm.26814 Copyright 2018 Wiley.

Figure 2 is adapted with permission from (1) Komlosh, M. E., Özarslan, E., Lizak, M. J., Horkay, F., Schram, V., Shemesh, N., Cohen, Y. and Basser, P. J. (2011), Pore diameter mapping using double pulsed-field gradient MRI and its validation using a novel glass capillary array phantom. Journal of Magnetic Resonance, 208: 128–135. doi:10.1016/j.jmr.2010.10.014 Copyright 2011 Elsevier; (2) von dem Hagen, E. A. and Henkelman, R. M. (2002), Orientational diffusion reflects fiber structure within a voxel. Magnetic Resonance in Medicine, 48: 454–459. doi:10.1002/mrm.10250 Copyright 2002 Wiley; (3) Fieremans, E., De Deene, Y., Delputte, S., Ozdemir, M. S., D'Asseler, Y., Vlassenbroeck, J., Deblaere, K., Achten, E. and Lemahieu, I. (2008), Simulation and experimental verification of the diffusion in an anisotropic fiber pha ntom. Journal of Magnetic Resonance, 190(2): 189–199. doi:10.1016/j.jmr. 2007.10.014 Copyright 2008 Elsevier; (4) Guise, C., Fernandes, M. M., Nóbrega, J. M., Pathak, S., Schneider, W. and Fangueiro, R. (2016), Hollow Polypropylene Yarns as a Biomimetic Brain Phantom for the Validation of High-Definition Fiber Tractography Imaging. ACS Applied Materials & Interfaces, 8(44): 29960–29967. doi:10.1021/acsami.6b09809 Copyright 2016 American Chemical Society.

Figure 3a, b and d is reprinted from Fieremans, E. (2008), Validation methods for diffusion weighted magnetic resonance imaging in brain white matter. (dissertation (monograph)), Ghent University (Fieremans, 2008).

Figure 5 is adapted with permission from (1) Baete, S. H., De Deene, Y., Masschaele, B. and De Neve, W. (2008), Microstructural analysis of foam by use of NMR R2 dispersion. Journal of Magnetic Resonance, 193(2): 286–296. doi:10.1016/j.jmr.2008.05.010 Copyright 2008 Elsevier; (2) Chin, C., Wehrli, F. W., Hwang, S. N., Takahashi, M. and Hackney, D. B. (2002), Biexponential diffusion attenuation in the rat spinal cord: Computer simulations based on anatomic images of axonal architecture. Magnetic Resonance in Medicine, 47: 455–460. doi:10.1002/mrm.10078 Copyright 2002 Wiley; (3) Fieremans, E., Novikov, D. S., Jensen, J. H. and Helpern, J. A. (2010), Monte Carlo study of a twocompartment exchange model of diffusion. NMR in Biomedicine, 23: 711–724. doi:10.1002/ nbm.1577 Copyright 2010 Wiley; (4) Harkins, K. D. and Does, M. D. (2016), Simulations on the influence of myelin water in diffusion-weighted imaging. Physics in Medicine & Biology, 61(13): 4729–4745. https://doi.org/10.1088/0031–9155/61/13/4729 © Institute of Physics and Engineering in Medicine. Reproduced by permission of IOP Publishing. All rights reserved; (5) Li, J. R., Nguyen, H. T., Nguyen, D. V., Haddar, H., Coatleven, J. and Le Bihan, D. (2014), Numerical study of a macroscopic finite pulse model of the diffusion MRI signal. Journal of Magnetic Resonance, 248, 54–65. doi:10.1016/j.jmr.2014.09.004 Copyright 2014 Elsevier; (6) Lin, M., He, H., Schifitto, G. and Zhong, J. (2016), Simulation of changes in diffusion related to different pathologies at cellular level after traumatic brain injury. Magnetic Resonance in Medicine, 76: 290–300. doi:10.1002/mrm.25816 Copyright 2016 Wiley; (7) Nguyen, D. V., Li, J.-R., Grebenkov, D. and Le Bihan, D. (2014), A finite elements method to solve the Bloch–Torrey equation applied to diffusion magnetic resonance imaging. Journal of Computational Physics, 263: 283–302. doi:10.1016/j.jcp. 2014.01.009 Copyright 2014 Elsevier; (8) Palombo, M., Ligneul, C., Hernandez-Garzon, E. and Valette, J. (2017), Can we detect the effect of spines and leaflets on the diffusion of brain intracellular metabolites? NeuroImage. doi:10.1016/j.neuroimage.2017.05.003 Copyright 2017 Elsevier; (9) Panagiotaki E., Hall M. G., Zhang H., Siow B., Lythgoe M. F., Alexander D. C. (2010), High-Fidelity Meshes from Tissue Samples for Diffusion MRI Simulations. In: Jiang T., Navab N., Pluim J. P. W., Viergever M. A., Medical Image Computing and Computer-Assisted Intervention. MICCAI 2010. Lecture Notes in Computer Science, vol 6362. doi: 10.1007/978–3-642–15745-5_50 Copyright 2010 Springer; (10) Xu, T., Foxley, S., Kleinnijenhuis, M., Chen, W. C. and Miller, K. L. (2018), The effect of realistic geometries on the susceptibility-weighted MR signal in white matter. Magnetic Resonance in Medicine, 79: 489–500. doi:10.1002/mrm.26689 Copyright 2018 Wiley.

Abstract

Phantoms, both numerical (software) and physical (hardware), can serve as a gold standard for the validation of MRI methods probing the brain microstructure. This review aims to provide guidelines on how to build, implement, or choose the right phantom for a particular application, along with an overview of the current state-of-the-art of phantoms dedicated to study brain microstructure with MRI. For physical phantoms, we discuss the essential requirements and relevant characteristics of both the (NMR visible) liquid and (NMR invisible) phantom materials that induce relevant microstructural features detectable via MRI, based on diffusion, intra-voxel incoherent motion, magnetization transfer or magnetic susceptibility weighted contrast. In particular, for diffusion MRI, many useful phantoms have been proposed, ranging from simple liquids to advanced biomimetic phantoms consisting of hollow or plain microfibers and capillaries. For numerical phantoms, the focus is on Monte Carlo simulations of random walk, for which the basic principles, along with useful criteria to check and potential pitfalls are reviewed, in addition to a literature overview highlighting recent advances. While many phantoms exist already, the current review aims to stimulate further research in the field and to address remaining needs.

Keywords

Numerical phantoms; Hardware phantoms; Validation; Microstructure; Brain

1. Introduction

With the nominal resolution of human MRI being limited to the millimeter level, research efforts in microstructural imaging have been shifted to biophysical modeling of the MRI signal in terms of the underlying microstructural properties of the biological tissue of interest. Along with the exponential growth of the field of microstructural imaging (Novikov et al., 2018), the need for its validation has become increasingly important. This review is dedicated to phantoms for the validation of microstructural MRI methods in the brain that are described elsewhere in the current Special Issue (Does, 2018; van Zijl et al., 2018) and in (Jelescu and Budde, 2017; Novikov et al., 2016). While phantoms for quantitative MRI in general have been recently reviewed (Keenan et al., 2018; Selwyn, 2014), the focus here is on what makes phantoms relevant for microstructural MRI. Most microstructural phantoms are currently used for the validation of diffusion MRI (dMRI), though magnetic susceptibility, magnetization transfer (MT) and intra-voxel incoherent motion (IVIM) are also microstructural effects of interest discussed here.

Both physical and numerical phantoms will be reviewed here in terms of their characteristic requirements, and how they can serve for validation of microstructural imaging, a critical and necessary step to enable microstructural quantification in normal subjects and patients. Specifically, we aim for microstructural phantoms that can serve for validating the range of biophysical models developed so far to describe the brain in health and disease. While such phantoms are potentially very useful by providing a so-called ground-truth of the brain microstructure, developing them can be challenging. Physical phantoms, on the one hand, typically cannot reproduce all the complexity of *in vivo* tissue, and their MR images tend to have pronounced artifacts due to unknown material properties being overlooked. Numerical

simulations, on the other hand, often do not match with physical (*in vivo* or phantom) measurements due to ignoring any other biophysical effects than the one(s) being simulated. Our aim here is to provide an overview of existing phantoms as well as guidelines on how to choose or manufacture a synthetic or numerical microstructural phantom that addresses the needs of a given project.

While experimental MRI sequence testing specifically requires physical phantoms, validation of biophysical models and fiber tracking algorithms can make use of both physical and numerical phantoms. Complementary to physical phantoms, numerical or software phantoms offer a controlled and flexible tool to simulate the effect of diffusion, MT and magnetic susceptibility variations on the MR signal in a known microstructural geometry. We focus here on Monte Carlo (MC) simulations, as this method really enables to go down to the microstructural level, and offers the greatest flexibility in terms of simulating different MR contrasts and realistic microgeometries. General guidelines and potential pitfalls are considered, along with an overview of different numerical phantoms employed for the validation of microstructural MRI so far.

2. Physical phantoms to validate brain microstructure

The term physical or hardware “phantom” is used here for well-characterized objects in terms of size and composition, that can be used for evaluating the accuracy and precision of MRI methods to study brain microstructure. Given this definition, the main focus will be on non-biological, man-made phantoms, with the exception of a brief discussion on the use of simple biological phantoms (based on food) for validation of MRI. While biological tissue is typically not well-characterized, appropriately engineered biological tissue can be very useful for validating microstructural features, which is discussed further in the Discussion, and in detail elsewhere in this Special Issue and in (Jelescu and Budde, 2017).

To provide both a systematic and practical overview, the requirements for a microstructural phantom of the brain are outlined here, followed by describing the characteristics of the main components (ingredients) of such phantom: a (NMR visible) liquid and additional (NMR invisible) substances or materials that induce a desired microscopic effect. We also present an overview of current hardware phantoms used in diffusion, IVIM, MT, and susceptibility weighted imaging.

2.1 Physical Phantom Requirements

When searching for a hardware phantom suitable for the validation and testing of microstructural imaging of the brain, the following requirements can be considered as minimally required:

(1) The phantom exhibits “microstructural” properties that affect the NMR properties of the liquid molecules on the microstructural scale, resulting in, e.g., restricted or hindered diffusion, MT, or local field inhomogeneities due to magnetic susceptibility differences. Furthermore, the phantom demonstrates realistic microstructural properties similar to as observed in the brain. Realistic bulk MR properties similar to those observed in the brain can be achieved

empirically by doping a water or gel such that the measured microstructural parameters of interest, in terms of diffusion, relaxation, susceptibility and MT, are similar to those parameters as measured in the brain. More fundamentally, the goal would be to create a phantom with a similar micro-environment as the brain, which is typically far from trivial to obtain. Often this is due to practical limitations, e.g., the quest is still ongoing for hollow fibers with a diameter of less than one micron to mimic axons. But there are also more fundamental reasons, as the actual brain microstructural properties (e.g., intra-, extra-cellular diffusivities, compartment fractions, magnetic susceptibility of myelin, etc.) are not very well-known in normal condition, let-alone in case of pathology.

(2) The phantom is well-characterized, especially in terms of its "microstructural properties", i.e. sizes, magnetic susceptibility, surface relaxation, etc. This often implies characterization using orthogonal imaging methods, including other MRI modalities, as well as other (ideally non-destructive) 3D high resolution imaging methods, based on light, electron or atomic force microscopy or using X-ray (a detailed comparison of available techniques is in table 2 of (Goggin et al., 2016)).

In addition to the ones above, other requirements, as listed in (Keenan et al., 2018; Tofts, 2004; Tofts et al., 2000) and the following below may further increase the usefulness of a microstructural phantom:

(3) The phantom materials are easily obtainable, cheap, stable and nontoxic. It should be noted that phantoms made of organic materials are not ideal from this perspective, though could be kept much longer when doped with very small concentrations of acute toxic compounds such as sodium azide (NaN_3) (Deene et al., 2000), Thiomersal (INN), Germall-plus® (Ernest et al., 2005) or antimicrobial or antifungal preservatives such as diazolidinyl urea (Lavdas et al., 2013), which on their turn may alter the toxicity and limit its use in clinical settings.

(4) The phantom is easy to assemble and can be made reproducible. This requirement along with requirement (1) of phantom features covering a range of realistic parametric values are particularly important in longitudinal and multi-site trials, where phantoms may be used to calibrate microstructural MRI methods. To illustrate this point, a study using a standardized apparent diffusion coefficient (ADC) phantom based on polyvinylpyrolidone (PVP) solutions at 0˚C (Boss et al., 2015; Keenan et al., 2018; Palacios et al., 2017) showed inter-scanner reproducibility of < 6% among 5 different sites, 2 field strengths, and 3 vendors (Boss et al., 2015). Another study using an ice-water phantom showed a coefficient of variation for the diffusion coefficient D of 3% among 8 different scanners, 5 sites, 2 field strengths and 2 vendors (Grech-Sollars et al., 2015). This implies that phantoms to test inter-scan and inter-site reproducibility should be stable and ideally have an even better reproducibility, making (pure) liquids therefore arguably the most suitable phantoms in this case.

Indeed, while (pure) liquids are typically not featuring microstructural properties, more crucial are the requirements of having high stability, reproducibility and being very well-characterized, particularly when performing large multi-site comparisons where sharing the same phantoms among all sites is not practically feasible. In particular, one should consider a phantom that is able to generate a signal (decay) that covers (at least) the same range as compared to the microstructural MRI measurement of interest. For the example of dMRI, a pure liquid exhibits a mono-exponential signal decay from which it will, depending on the chosen D, start to deviate when approaching the noise floor for sufficiently high diffusion weighting or b-value. Comparing the directional signal decays among different scanners can then reveal accuracies in gradients or b-value calibration, and differences in noise floor and image reconstruction (adaptive combine versus sum of squares combination techniques). Next, the effect of signal-to-noise ratio (SNR) on estimation of the microstructural parameters of interest can then be further evaluated using numerical simulations of noise propagation.

While the ideal microstructural phantom mimicking brain and fulfilling all the criteria above may currently not exist, there is an increasing number of phantoms being proposed for the validation of microstructural experiments, particularly for dMRI. Next, we discuss the basic components of those phantoms.

2.2 Phantom Components

Physical phantoms consist of an NMR visible liquid (i.e. resulting in signals by using an MRI sequence with particular parameter settings including TE and TR) that may serve as a phantom on its own, or often is doped with or used for immersing an NMR invisible material in to induce the desired microstructural properties. Here, we will discuss and illustrate the critical factors of both the NMR visible liquids and NMR invisible materials, that determine the SNR and microstructural properties of a phantom, separately.

NMR visible liquids—Pure liquids exhibit isotropic Gaussian diffusion and are characterized with a well-established (timeindependent) diffusion constant. While just simple liquids are useful as a standard for quality assurance (QA) when calibrating diffusion protocols and evaluating new diffusion sequences and post-processing methods, they also form the basic component of microstructural phantoms when used for immersing microstructurally confined (NMR-invisible) materials. Several characteristics of liquids should be taken into account when using liquids as the main component of (microstructural) phantoms:

(1) The **diffusion coefficient D**, depending on the viscosity, molecular size (mass) and temperature (cf. Figure 1 for H_2O), affects the diffusion properties of the phantom.

(2) The **longitudinal T_1** (Gowland and Stevenson, 2004) and **transverse T_2** (Boulby and Rugg–Gunn, 2004) relaxation times of the liquids define an upper bound for the maximal possible SNR of the measurement, as combining the liquids with other (NMR invisible) materials may further shorten relaxation

times due to surface relaxation and local field inhomogeneities, as discussed below. T_1 increases with static magnetic field strength, while T_2 in pure liquids is not expected to change with magnetic field strength (Bloembergen et al., 1948). In addition, D, T_1 and T_2 values depend on the temperature (cf. Figure 1 for H_2O) and typically change 1–3%/˚C, and without special precautions, MRI measurements based on these properties are subject to an uncertainty of about 2˚C, corresponding to errors of about 5% in the parameter values (Tofts, 2004).

(3) The proton NMR spectrum of the liquid (Bovey et al., 1988), in particular, the presence of **single or multiple proton NMR spectral lines**, is important to consider, as the latter can result in chemical shift artifacts, as illustrated in Figure 1 for linear alkanes (dodecane and n-tridecane) when using echo-planar imaging (EPI). Alternatively, multiple spectral lines can also be employed as an internal temperature probe (Spees et al., 2012) or to create multi-compartment phantoms for diffusion (Fieremans et al., 2012b) or relaxation (Ababneh et al., 2004).

NMR invisible materials—Phantom materials are used either for doping or immersing in the liquid to induce microstructural properties that can be measured with MRI, e.g., by restricting the diffusion over micron length scales, or by magnetic susceptibility and surface relaxation effects, thereby creating a true microstructural phantom. Following properties of the phantom material, combined with the liquid properties, then determine the overall characteristics of the microstructural phantom:

(1) Dimensions: Brain microstructural phantoms ideally exhibit features (either restricting the diffusion, inducing magnetic susceptibility differences, MT, or additional T_2 relaxation) over length scales similar as observed in the brain. The dimensions are particularly important for diffusion phantoms, with dMRI probing length scales $\sim\sqrt{Dt}$, with the diffusion time of the experiment. With standard monopolar diffusion weighting (Stejskal, 1965), is typically < 50 ms, hence a phantom with restrictions over length scales ~ 10 μm filled with water ($D \approx 2$ μm^2/ms at room temperature) will give contrast on dMRI using conventional sequences. Increasing using stimulated echo diffusion weighting (Merboldt et al., 1985; Tanner, 1970) consequently enables probing longer by varying mixing time without the need of increasing TE and might be considered for phantoms with larger “microstructural” dimensions.

In brain, typical length scales range from less than 1 micrometer for cell organelles and inner axon diameters (Aboitiz et al., 1992; Caminiti et al., 2013; Caminiti et al., 2009; Innocenti et al., 2015) to tens of micrometers for neurons and correlation lengths of cell and axon packings. This (sub) micrometer resolution is what makes realistic microstructural imaging phantoms often quite challenging, both for manufacturing and characterization.

For manufacturing, 3D printing (also known as rapid prototyping or additive manufacturing) has been proposed for medical imaging phantoms (Bieniosek et al., 2015), though the technology is currently not available yet for manufacturing microstructural phantoms because of achievable resolution and/or scalability. In particular, commercially available

polyjet 3D printers can jet layers of liquid photopolymers as thin as 16 microns to build complex models with a resolution (typically multiple layers thick) that is still much larger than the brain microstructure. Alternatively, steriolithography (SLA) methods using dedicated laser technology (Anscombe, 2010), either subtractive or additive, offer a higher resolution (up to submicron), though a potential issue is scalability of this technology to produce samples with macroscopic size big enough to image with MRI.

(2) Magnetic Susceptibility: Local variations in magnetic susceptibility χ due to differences between the liquid and the phantom material induce a local inhomogeneous field. If the magnetic properties of the phantom are well-characterized, it may serve to test and validate quantitative susceptibility imaging (Bowtell et al, special issue). Magnetic susceptibility differences, however, are often not well characterized, and also affect other microstructural parameters: In particular, the local variations in χ cause additional mesoscopic (Kiselev and Novikov, Special Issue) T_2 relaxation (Borgia, 1996; Jensen and Chandra, 2000a, b; Kiselev and Posse, 1999; Novikov and Kiselev, 2008; Weisskoff et al., 1994; Yablonskiy and Haacke, 1994). Furthermore, they may cause distortion artifacts, and the corresponding internal gradients could compromise the accurate determination of diffusion parameters (Does et al., 1999; Farrher et al., 2017; Kiselev, 2004; Laun et al., 2009; Pampel et al., 2010; Zheng and Price, 2007; Zhong et al., 1991). Note that these effects will depend on the magnetic susceptibility differences, the phantom geometry and corresponding correlation length over which they are played out, as well as the B_0-field, and the employed NMR sequence (gradient-echo or spinecho with given TE), all determining the specific regime (diffusion narrowing versus static dephasing), as explained in detail by Kiselev and Novikov in this Special Issue.

As an illustration, for a crossing fiber phantom, the observed SNR and precision on diffusion parameter estimation can vary between the individual (identical) bundles, as the B_0-field inhomogeneity depends strongly on the orientation of each bundle with respect to the static B_0-field (more parallel orientation results in more uniform B_0-field and corresponding higher SNR).

To reduce the unwanted effects on the SNR and diffusion properties, χ-differences within the phantom should be minimized. (Wapler et al., 2014) measured the magnetic susceptibility difference from water, $\left(\chi - \chi_{H_2O}\right)$, of many widely-used materials in MR engineering and MR microtechnology and present a comprehensive overview of available susceptibility data. They conclude that several materials with various physical properties are available with $\left(\chi - \chi_{H_2O}\right)$ below ±0.3 ppm, with PMMA the most MR-compatible material, $\left(\chi - \chi_{H_2O}\right) \approx 0.02 - 0.04$ ppm.

Alternatively, susceptibility matching can be obtained by doping the liquid. In the case of water ($\chi_{H_2O} = -9.05$ppm), when the phantom material χ is larger (less diamagnetic), the water can be doped with paramagnetic contrast agents to match the susceptibility, as previously proposed to reduce line broadening in spectroscopy measurements (Stoll and

Majors, 1982). Similarly, when the phantom material χ is lower (more diamagnetic) than water, the water can doped with salt (Farrher et al., 2017; Laun et al., 2009). By doing this, the relaxation rates and conductivity are potentially altered as well.

(3) Surface Relaxation: The partial absorption of magnetization to the wall or surface has been studied in the field of porous media (Kleinberg, 1996; Mitra et al., 1993; Sen et al., 1994), and its effect can be characterized by the material's surface relaxivity ρ, which has dimensions of velocity, as it describes the strength of the interaction between the material surface and the fluid.

While surface relaxation is typically not considered or the surface relaxivity is not described, it can alter the SNR, diffusion properties and MT effects of microstructural phantoms. Surface relaxation always causes additional T_2-decay, $R_{2,\mathrm{surf}} = \rho\frac{S}{V}$ (Kleinberg, 1996), with $\frac{S}{V}$ the surface-to-volume ratio, resulting in SNR loss. Its effect on diffusion is not universal and depends on the specific microstructural geometry and the diffusion time; In general, D increases due to surface relaxation at short times (Mitra et al., 1993), whereas it typically decreases at long times except for the case of specific confined geometries such as dead spaces (Sen et al., 1994). The effect of surface relaxation on T_2 depends on the amount of surface, $\sim\frac{S}{V}$, and this dependency can be quite significant, as illustrated in (Fieremans et al., 2008a) for fiber phantoms made of different materials and densities.

To minimize the (typically unknown) effects of surface relaxation, materials with a low may be more suited when making microstructural phantoms. In the case of water, ρ is related to the water wettability (Chen et al., 2006; Schrader, 1992), defined by the contact angle between a droplet of fluid on a horizontal surface in thermal equilibrium (Yuan and Lee, 2013), with a lower contact angle indicating a more hydrophilic material and correspondingly more surface relaxation. Hence, to minimize the effect of surface relaxation, hydrophobic phantom materials may be most appropriate. On the other hand, hydrophilic materials may be preferred to avoid the presence of air bubbles (causing internal gradients due to susceptibility mismatch). This issue can be minimized by making phantoms under water, and removing remaining bubbles using vacuum chambers and ultrasonic baths (Fieremans et al., 2008a).

(4) Proton Density: The phantom SNR is determined by its proton density and the T_1 and T_2 relaxation times of the liquid (influenced by the NMR invisible phantom materials, as described above). The proton density in microstructural phantoms depends on the amount of NMR visible and invisible materials and is typically much lower than in brain due to, e.g., the use of plain fibers rather than hollow fibers or the use of capillaries with thick walls. The loss in signal due to the decrease in proton density can be compensated by using liquids with longer relaxation times compared to *in vivo* brain. As an example: for a phantom mimicking white matter (WM) with a given proton density $PD_{ph} = 0.3$, in order to obtain similar SNR at a given TE of 100 ms as *in vivo*, the corresponding T_2 in the phantom should be $T_{2,ph} \approx -TE/\ln\left(\frac{PD_t}{PD_{ph}}\exp\frac{-TE}{T_{2,t}}\right) \approx 200$ ms, assuming the proton density of tissue water, 2, in brain WM is about 65 % (Tofts, 2003) with a corresponding $T_{2,\mathrm{t}}$ of about 80 ms at 3T.

Furthermore, as the other properties described in (2) and (3) may further lower the T_2 and resulting SNR, deionized water with no additional doping is often used as an MR-visible component in microstructural phantoms.

2.3 Examples

An overview based on literature is given here of the current state-of-the-art on phantoms used for diffusion, IVIM, susceptibility and MT, respectively, along with their applications. While some materials (e.g., gels and doped liquids) are used as phantoms for different modalities simultaneously, the majority of them are predominantly used for one modality, in particular diffusion.

Diffusion phantoms: Diffusion phantoms exist with increasing complexity ranging from liquids (see Figure 1, Table 1), to advanced microstructural phantoms mimicking brain (Figure 2, Table 2) and plants (e.g., Figure 3).

Liquids: **Water** is the universal test liquid used for MRI, due to its properties of being inert, stable and readily available. Potential drawbacks of water are its low viscosity, making it prone to vibrational artifacts, its intrinsic long T_1- and T_2-values on the order of 1 s or more, depending on the dissolved oxygen, and its relative high diffusion coefficient (2 μm^2/ms, cf. Figure 1) at room temperature compared to those values in brain, e.g., at 3T for WM T_1 ~ 700–800 ms, T_2 ~ 80–110 ms (Oros-Peusquens et al., 2008; Wansapura et al., 1999), and mean diffusivity ranging 0.3 – 1 μm^2/ms (Tofts, 2004). At 0˚C, ice-water has a D of 1.1 μm^2/ms (Easteal et al., 1989), and when surrounding it by an insulating bath filled with ice and water, it has been shown useful as a temperature-controlled fluid in ADC phantoms in multi-center studies (Chenevert et al., 2011; Grech-Sollars et al., 2015; Malyarenko et al., 2016; Mulkern et al., 2015). Furthermore, (distilled) water is also by far the most commonly used fluid inside microstructural phantoms, where the long intrinsic T_1- and T_2-values are typically helping to have a reasonable SNR, as the proton density in such phantoms is typically much lower, and surface relaxation and local susceptibility differences cause additional T_2(*) relaxation.

More pure liquids and their corresponding temperature dependency are listed in (Holz et al., 2000). Particularly the **alkanes**, both cyclic and linear, have been proposed as an alternative for water because of a relative low D at room temperature as compared to water (Table 1, Dowell and Tofts, 2010), though they have other disadvantages such as toxicity and multiple spectral lines for linear alkanes (illustrated in Figure 1). In addition, silicon oils and polymers are commonly used to test for gradient calibration (Price, 2009; Spees et al., 2012), including ethylene glycol and decamethylcyclopentasiloxane, also known as D_5, both having a low diffusion coefficient (cf. Table 1).

Aqueous solutions proposed to mimic diffusion in brain are listed in Table 1 (including diffusion properties and potential (dis)advantages) and demonstrated in Figure 1. Commonly used are solutions with sucrose (Table 1), polyvinylpyrolidone (PVP, Table 1), and agar gels. Aqueous solutions with human serum albumin have also been characterized in terms of their diffusivity and relaxation values (Fukuzaki et al., 1995). It should be noted that the diffusion properties of protons in aqueous solutions may not be Gaussian and thus may demonstrate

diffusion time-dependence, e.g., in the case of sucrose solutions (Hara et al., 2014; Wang et al., 2017). **Gels** created by varying concentrations of agar (or other gelling agents (Hellerbach et al., 2013)), contrast agents, and sucrose, are popular phantoms as they create the possibility of varying values of T_1, T_2 and D independently (Laubach et al., 1998; Lavdas et al., 2013).

Mixtures, e.g., based on acetone and water have been proposed (Wang et al., 2017), whereby the D of acetone decreases due to hydrogen-bond strengthening, and the NMR spectrum of this phantom can be reduced to a single peak (acetone) by replacing water (H_2O) with deuterium oxide (D_2O). The entire physiological range can be obtained by varying the concentration of the solute, as illustrated in Figure 1.

Dairy **cream** is an oil-in-water emulsion that, due to its two distinct components, has found application as an isotropic phantom both for bi-exponential T_2 relaxation (Jones et al., 1998) and diffusion (Ababneh et al., 2004; Fieremans et al., 2012b) mimicking brain WM. In particular, the protons from the triglycerides of the fat globules in cream were found to be responsible for a very slow diffusing component, proportional to the percentage of milk fat, with a short T_2 of about 38 ms, whereas the water protons were responsible for a fast diffusion component with a longer T_2 of about 135 ms (Jones et al., 1998). When heating the cream prior to imaging, the fat T_2 increases and water T_2 decreases, which, for TEs typically used in clinical dMRI protocols, results in D of 1.1 $\mu m^2/ms$ and diffusion kurtosis K of 1.2, similar to values observed in brain WM (Fieremans et al., 2012b). Furthermore, as shown in Figure 1, the fat-water frequency shift can be utilized to visualize both water and fat separately (using, e.g., echo-planar imaging), and serve to predict the values of the two components added together.

Liquid crystals consisting of water, detergent (sodium dioctyl sulfosuccinate, Aerosol-OT), and isooctane have been used to create phantoms exhibiting (microscopic) anisotropy, due to the self-assembled detergent aggregates hindering the translational motion of the water molecules (Nilsson et al., 2018). The proposed phantom (illustrated in Figure 1) requires preparation by mixing the components and mild heating followed by cooling to room temperature, after which it is thermodynamically stable, with diffusion properties suitable for testing dMRI methods, i.e. mean diffusivity comparable to brain tissue, arbitrary values of fractional anisotropy (FA), and microscopic FA equal to the theoretical maximum of 1.

Anisotropic microstructure phantoms: **Microcapillaries** (see Table 2 and Figure 2) are used to simulate restricted diffusion and create anisotropic phantoms useful for testing new diffusion sequences, as well as validating pore size mapping methods using dMRI. Such phantoms consist of hollow fiber systems that are made from glass or plastic with an internal diameter (I.D.) ranging from 1 – 50 μm, and external outer diameters (O.D.s) of 75 μm or more (cf. Table 2). Capillary phantoms with a well-known I.D. serve as phantoms to study the diffusion in the intra-axonal space (in which case the capillaries are immersed in NMR invisible fluids such as fomblin, fluorinert, deuterated 1,2-dichlorobenzene), and have been used to evaluate axonal diameter mapping using single and double pulsed-field-gradient methods (see Table 2 for references). Yet, the capillary I.D. as listed in Table 2 are larger

than the values observed for axon diameter from histology (Aboitiz et al., 1992; Caminiti et al., 2009; Innocenti et al., 2015).

Experimentally, potential issues with capillary phantoms could be low signal in the case of low ratios of I.D./O.D, and filling the capillaries with water without the presence of air bubbles. Capillary action, occurring when the adhesion to the surface material is stronger than the cohesive forces between the water molecules, enables the fluid, e.g., water, to get into the capillary, and is limited by surface tension and gravity. For hydrophilic surfaces, the tension is small, which will enhance capillary action and get water into the tube, while hydrophobic surfaces increase surface tension, hence will make it harder for water to get into the capillaries. From this perspective, it is beneficial to have capillaries made of a hydrophilic material, which makes it relatively straightforward to fill them with water and remove air bubbles. On the other hand, hydrophilic materials also have increased NMR surface relaxation (Chen et al., 2006), resulting in a decrease in T_2 for the water inside hydrophilic capillaries, which will lower the overall SNR of the dMRI experiment, as well as potentially affect the diffusion properties, as discussed in Section 2.2.

Glass capillary arrays (GCAs) phantoms, (Figure 2 and Table 2) as proposed by (Benjamini et al., 2014; Komlosh et al., 2017; Komlosh et al., 2011)), consist of capillaries (with I.D. of 10 μm) that are tightly packed hexagonally with no fluid in between, thereby maximizing the signal from within the capillaries. A three-step procedure using controlled activity of water vapor has been proposed to fill the GCAs with water (Komlosh et al., 2011) or decamethylcyclopentasiloxane (Komlosh et al., 2017).

Hollow fibers have been recently proposed to manufacture so-called biomimetic phantoms given their ability to more closely mimic microstructure. Hollow aligned fibers with an adjustable size distribution, created using electrospinning with cyclohexane infused into the pores, have been used to create inner axon-like structures with I.D. ranging from 9.5 – 13.4 μm (Hubbard et al., 2015) (a similar phantom has also been proposed for cardiac dMRI (Teh et al., 2016)). In addition, hollow polypropylene yarns, also dubbed ‘taxons’ with an I.D. of about 12 μm and O.D. of 34 μm, have been proposed to represent WM microstructure by mimicking both intra- and extra-axonal space, and used to study the effect of dispersion and crossings on fiber tracking (Guise et al., 2016), as well as very recently to validate compartment size and fraction measurements (Fan et al., 2018).

Plain (solid/non-hollow) fibers with an O.D. of 10 – 20 μm have also been used frequently as anisotropic phantoms (see Table 2, Figure 2), for quality assurance and testing of diffusion sequences, as well as for evaluating diffusion fiber tracking algorithms (Fillard et al., 2011). Based on the criteria listed above, the microstructural properties depend on the fiber material (magnetic susceptibility, and hydrophobic versus hydrophilic), the fiber diameter and the fiber density. We previously performed a detailed comparison of several fibers in terms of their microstructural diffusion properties (Fieremans, 2008; Fieremans et al., 2008a), and concluded that the most appropriate fiber phantoms to mimic dMRI measurements in brain WM are densely packed fiber bundles made from a hydrophobic fiber material with a magnetic susceptibility close to water and sufficiently small diameter.

Several ways have been proposed to pack the fibers tightly enough to give rise to anisotropy, including the use of shrinking tubes.

Plain fiber bundles serve as a phantom to model the extra-axonal space, and have been used to study the effect of axonal packing geometry on the (time-dependent) diffusion coefficient (Burcaw et al., 2015), as well as to validate the short-time limit (Latour et al., 1994; Mitra et al., 1993) using oscillating gradients diffusion weighting schemes (Lemberskiy et al., 2017).

While most anisotropic phantoms are cylindrical, **planar phantoms** can also be created by stacking thin plates in 1*d*. Such phantoms have been described either consisting of 100 μm thick glass plates with 20 μm in between to calibrate the b-matrix in dMRI (Kłodowski and Krzyżak, 2016; Krzyżak and Olejniczak, 2015), or consisting of permeable membranes to study exchange, described further below.

Isotropic microstructure phantoms: Compared to the vast selection of anisotropic microfiber phantoms described in literature, relatively fewer microscopically restricted isotropic phantoms have been proposed. These include yeast suspensions, described in the next section, and cross-linked dextran gels, consisting of beads with a size discretely ranging over 20–300 μm (sephadex™), which have been used in dMRI (Liang et al., 2017; Magin et al., 2011) as well as for testing IVIM and susceptibility weighted imaging, both discussed below. Other employed phantoms include packings of poly(ethyl methacrylate) beads with a diameter of 42 μm (Koch and Finsterbusch, 2008), and styrene beads with diameters of 0.05, 5, 6, and 10 μm (Capuani et al., 2013).

Permeable microstructure phantoms: Most microstructural phantoms proposed in literature consist of multiple compartments with typically impermeable walls (or a permeability that is not well known). In addition to red blood cells (Latour et al., 1994; Stanisz et al., 1998) and yeast, as discussed in the next section, recently, a dedicated hardware phantom has been proposed consisting of a 1*d* stack of polycarbonate films made permeable by punching holes with a tunable submicron size, and used to study the time-dependent diffusion (Papaioannou et al., 2017).

Simple biological phantoms: Certain food, plants and fruits (Hills, 1998) that are widely available have been used as test-objects for MRI and reviewed here briefly, with an in-depth overview of phantoms based on biological tissue being beyond the scope of this review. Monocotyl plants or monocots such as **celery** (Apium graveolens) and **asparagus** (Asparagus officinalis) are described in the literature to evaluate the effect of inhomogeneous susceptibility on dMRI (Neeman et al., 1991; Trudeau et al., 1995) and as anisotropic dMRI phantoms (Baete et al., 2013; Boujraf et al., 2001; Lätt et al., 2007; Panagiotaki et al., 2010; Sigmund and Song, 2006). Figure 3 shows a microscopic image of a cross-section through the inner part of the asparagus, composed of parenchyma in which vascular bundles are embedded. There is an increase in size of vascular bundles towards the center of the stem. Figure 3 shows a close-up of a vascular bundle, consisting of the phloem (smaller cells, either tubular filled with air, or spherical filled with water) and xylem (long tubular cells with a thick wall), with the latter exhibiting anisotropic diffusion. The resulting dMRI parametric maps and fiber tract are shown in Figure 3. While widely available, the

low degree of anisotropy, presence of air bubbles, and poor characterization (e.g., on exchange through the cell walls), limit the use of plants as microstructural phantoms, though they have shown to be useful to test dMRI sequences.

Yeast is a well-studied eukaryotic model organism that in suspension has been used as a twocomponent system featuring isotropic diffusion of both the intracellular and extracellular water with exchange in between. Yeast cells are spherical with a diameter of about 3 – 7 μm (Silva et al., 2002; Tanner, 1983), intracellular diffusivity of ~ 0.65 μm^2/ms at room temperature (Åslund and Topgaard, 2009), extracellular diffusivity depending on the packing density of the cell suspension (e.g., 1.2 μm^2/ms at room temperature for an intracellular fraction of 0.41), and exchange times measured to be in the range of 250 ms (Table VI in (Tanner, 1983)), and 280 ms in (Åslund et al., 2009). Since the first characterization by Tanner (Tanner, 1983; Tanner and Stejskal, 1968), yeast cell suspensions have been shown very useful as a simple well-characterized phantom to validate methods for assessing exchange, intracellular diffusion, and compartment shapes (Åslund et al., 2009; Åslund and Topgaard, 2009; Cory and Garroway, 1990; Eriksson et al., 2013; Lasič et al., 2011; Lasič et al., 2014; Shemesh et al., 2011; Shemesh et al., 2012; Silva et al., 2002). Interestingly, (Cheng and Cory, 1999) demonstrated (and verified under the microscope) that radiation treated yeast cells (whose DNA had lost its ability to duplicate) become pronouncedly prolate, whereby the eccentricities of the prolate cells are controlled by the culture times.

Finally, in addition to dairy cream described above, avian **egg latebra** presenting in the yolk has been shown to exhibit bi-exponential diffusion signal decay measured over the range up to b-value = 5 ms/μm^2, with diffusion parameters similar to those observed *in vivo* in human brain, and additionally, a very slow diffusing water component over the range up to a b-value of 50 ms/μm^2 (Maier et al., 2014).

IVIM Phantoms: Various phantoms have been proposed for the testing and validation of IVIM (Cho et al., 2012; Karampinos et al., 2010; Lee et al., 2016; Maki et al., 1991; Ohno et al., 2017). With the exception of cotton surgical sponges being used in which water flows under the influence of gravity (Lorenz et al., 1991), all other phantoms relied on programmable (peristaltic) pump systems. These are then used to pump water at various rates, e.g., through intramedic polyethylene tubing with I.D. 0.86 mm and O.D. 1.27 mm (Karampinos et al., 2010), or through a cellulose sponge (Cho et al., 2012), or through crosslinked dextran gels (sephadex™) (Bihan et al., 1988; Lee et al., 2016; Lorenz et al., 1991; Maki et al., 1991). In these gels, for packings made of gel beads consisting of particle sizes ranging from 20 up to 300 μm, pore sizes were obtained with a diameter of approximately 1 nm, mimicking the capillary fenestrations in the brain, (Lee et al., 2016). Another cranial phantom consisted of a high-density polypropylene filter (mimicking brain parenchyma) with intra- and extra-filter space (mimicking cerebral artery and vein, respectively), and a capacitor space (mimicking the cerebrospinal fluid space). Pulsatile and steady flow with different flow rates were applied to the cranial phantom using a programmable pump (Ohno et al., 2017).

While these phantoms provide a qualitative description of the IVIM effect, a challenge is to characterize and produce them in a controllably manner. Particularly to mimic the vascular

network, sacrificial sugar structures (i.e. melt-spun sugar fibers embedded in a block of epoxy resin) have been proposed for the evaluation of dynamic contrast-enhanced MRI (Gaass et al., 2017) and recently also for IVIM (using water injections with syringes for a controlled flow) (Schneider, 2016). Here, structural analysis was performed using light microscopy before the MRI to characterize the highly interconnected network of microchannels with diameters ranging from 2.5 – 25 μm.

Susceptibility Imaging Phantoms: **Doping water** with (super)paramagnetic metal based contrast agents such as nickel salt, copper sulfate, manganese chloride (Pan et al., 2011), gadolinium chelates (Chan and Wong, 2007), iron oxides, etc., is a frequently employed method to alter the T_1, T_2-values (see Table 3.5 in (Tofts, 2004)), as well as for inducing magnetic susceptibility effects (Deistung and Reichenbach, 2011) in phantoms.

Microstructural phantoms used for susceptibility imaging include **cross-linked dextran gels** (sephadex™) consisting of particles with a discrete wet bead size ranging from 20 up to 300 μm and a diamagnetic susceptibility different from water (Jensen et al., 2006), and gels consisting of ferric iron hydroxide dextran complex to mimic iron load (Chu et al., 2004). Recently, polystyrene microbeads with diameter discretely ranging between 11.3 and 42.2 μm suspended in an aqueous solution of sodium chloride doped with holmium(III) chloride hexahydrate have been used to investigate the dependence of the precession frequency on the medium microstructure, along with numerical simulations (Ruh et al., 2018).

Relevant for the brain WM, the orientation-dependent variation of the apparent magnetic susceptibility (Li et al., 2011) may originate from anisotropic magnetic susceptibility (described by a 2nd order tensor) of myelinated axons. Very recently, 25 or 70 μm thick **pyrolytic graphite sheet (PGS)** with a known large magnetic susceptibility anisotropy has been proposed to create phantoms in different shapes (slabs, spherical and cylindrical shells) (Cronin, 2016; Cronin and Bowtell, 2018), allowing to directly validate theoretical expressions of the magnetic field variation.

Magnetization Transfer Phantoms: Most studies to date have used either cross-linked bovine serum albumin (BSA) (Koenig et al., 1993), or **agar** gels (Henkelman et al., 1993; Mendelson et al., 1991) as phantoms to model MT effects. Heatdenaturated egg albumin (or boiled egg white) is also a straightforward way to manufacture phantoms with a strong MT effect (Yeung and Swanson, 1992).

Dedicated efforts early on have focused on **lipid membrane** systems to more adequately represent the MT effect observed in neural tissue (Grossman, 1999; van Zijl et al., 2018). Using mixtures of egg phosphatidylcholine (EPC)/cholesterol with pure EPC in the chloroform phase, cholesterol was shown to induce MT (Fralix et al., 1991), as well as shown to be a determinant of gray-white contrast in MRI of brain (Koenig et al., 1993). The MT properties of several other macromolecular solutions are listed in table 1 of (Ceckler et al., 1992). Furthermore, multi-lamellar vesicle suspensions of pure phosphatidylcholine with varying proportions of cholesterol, sphingomyelin, and galactocerebroside at varying pH values were used as synthetic WM lipids to demonstrate the importance of cerebrosides and pH on MT (Kucharczyk et al., 1994).

Recently, **lyotropic lamellar liquid crystals** (LLCs) have been proposed as surrogate biological membranes as they manifest a molecular arrangement common for some biological structures such as cell membranes and myelin sheaths, with MT between the water and the aliphatic (semisolid) components (Malyarenko et al., 2014). In addition to its similarity to biology, other advantages are stability, and simple phantom preparation or commercially being available as hair conditioner (Swanson et al., 2012). (Malyarenko et al., 2014) investigated the MT and relaxation properties of an LLC system composed of decanol, sodium dodecyl sulfate and water, and showed a clinically relevant range of semisolid fraction proportional to detected MTR. (Lee et al., 2017b) further investigated the mechanisms of MT in the same LLC by using deuterated molecules and single- and dual-frequency RF irradiations, to confirm that the decanol molecules are mainly responsible for the MT effects, through proton exchange to water.

3. Numerical phantoms for microstructure modeling

Numerical phantoms provide the flexibility to validate biophysical models and optimize NMR sequences under a wide range of acquisition parameters and tissue properties, thanks to the total control over phantom properties and the possibility of creating substrates mimicking specific biological tissue microstructure. Numerical simulations could be performed in several ways, based on (1) matrix formalisms, (2) finite-difference and finite-element methods, and (3) Monte Carlo (MC) simulations.

The matrix formalism relies on finding solutions for the eigenmodes of the diffusion propagator, and is computationally fast due to its implementation using matrix multiplications (Callaghan, 1997). Practically, these eigenmodes were only found analytically for diffusion within simple shapes, i.e. highly symmetric porous media, such as parallel planes, circles, spheres, cylinders (Callaghan, 1995), and their concentric multi-shell versions (Grebenkov, 2010; Lebois et al., 2013a, b). Furthermore, for contrast mechanisms other than diffusion, surface relaxation (Callaghan, 1995) and water exchange (Grebenkov, 2010, 2014), corresponding propagators could be very complicated and analytically intractable. To extend the applicability of the matrix formalism for a complicated geometry, the eigenmodes of corresponding Laplace equations can potentially be estimated numerically.

To numerically solve the mesoscopic Bloch-Torrey equations for complex micro-geometries with permeable membranes, finite-difference methods were proposed to simulate the diffusion either in artificially designed geometries (Harkins et al., 2009; Russell et al., 2012) or in realistic microstructure (Chin et al., 2002; Hwang et al., 2003). Also, Bloch-Torrey equations can be solved numerically by finiteelement methods for various geometries with impermeable (Hagslatt et al., 2003) or permeable membranes (Beltrachini et al., 2015; Li et al., 2014b; Moroney et al., 2013; Nguyen et al., 2014).

MC simulations are computationally expensive since they collect the ensemble average of numerous particles' random walks, resulting in statistically meaningful parameter estimates. Nonetheless, MC simulations are by far the most popular since they offer great flexibility to simulate diffusion along with other contrast mechanisms, e.g., water exchange, MT, surface

relaxation, susceptibility and T_1, T_2 relaxation, in all kinds of micro-geometries. In the following sections, we will review MC simulations for various physical phenomena, discuss minimum requirements and provide a checklist (Figure 4) for actual implementations, and list several examples.

3.1 How to simulate the physical phenomena in microstructure MRI?

Diffusion—The dMRI signal is simulated by initiating many particles in a microscopic geometry, propagating them in random directions, and calculating the resulting phase changes from random walks and corresponding diffusion gradients. The walkers can randomly hop on a pre-defined lattice or in a continuous space with a fixed step size or a step size dynamically adapted to local geometrical length scales (Grebenkov, 2011). Considering the balance between simplicity of the implementation and computational efficiency, we focus here on random-hopping in a continuous space with a fixed step size. According to the following statistical law derived by Einstein for Brownian motion (Einstein, 1905), the size of each step for each particle is approximated by

$$\delta x \simeq \sqrt{2dD_0 \cdot \delta t}, \quad \#(1)$$

where 7 is the dimensionality, D_0 is the intrinsic diffusion coefficient, and δt is the time spent for each step.

The single-step diffusion propagator is modeled by a binomial distribution in $1d$, a circle or a compressed ellipse in $2d$ (to mimic the multi-layer myelin sheath) (Harkins and Does, 2016), and a spherical surface in $3d$. A potential mistake in $3d$ simulations is to sample the step orientation over $\theta=\pi v$ and $\phi=2\pi u$ of a spherical coordinate, rather than over $\cos\theta=1-2v$ and $\phi=2\pi u$ (Fieremans et al., 2008b), with two uniformly distributed random numbers u, v between 0 and 1. The former implementation propagates particles towards the z-axis more than other directions, leading to overestimated diffusivities in z-direction and underestimated diffusivities in x- and y-directions; in contrast, the latter implementation propagates particles homogenously in all directions with the same probabilities. This sphere-point-picking problem can also be solved by sampling x, y and z of a Cartesian coordinate with three normally distributed random numbers.

dMRI signals under different diffusion weightings are simulated by varying the b-value $b \equiv \int |\boldsymbol{q}(t)|^2 dt$ where $\boldsymbol{q}(t) \equiv r \int \boldsymbol{g}(t')dt'$, with γ the gyromagnetic ratio of the water proton and $\boldsymbol{g}(t)$ the time-varying diffusion gradient. For each particle, the designed N() induces a phase change $\varphi = -\gamma \int \boldsymbol{g}(t) \cdot \boldsymbol{r}(t)dt$, where $\boldsymbol{r}(t)$ is the simulated diffusion trajectory. The corresponding simulated dMRI signal is then calculated by $S(\boldsymbol{g}) = \langle e^{i\varphi} \rangle$.

Each simulated diffusional trajectory is effectively a sample of the diffusion propagator. However, recording all trajectories needed to approach a reliable propagator estimate is very burdensome on memory storage. Furthermore, estimating the whole propagator exactly is also computationally very intensive, particularly in terms of its higher order moments or cumulants. Therefore, for all practical purposes, only physical quantities relevant for comparing with experiments are calculated for most MC simulations, which implies that the

propagator is sampled in finite order cumulants (e.g., up to 2 (Eq. 2), or up to 4 (Eq. 3)), and equivalently, dMRI signals are sampled in a finite range of q-space, naturally represented by the cumulant expansion (Kiselev, 2010).

For simulations of a conventional monopolar pulsed-gradient sequence with a very short diffusiongradient-pulse width, calculations of the diffusivity and other metrics related to higher order moments are straightforward: In this case, the diffusivity can be estimated by the second order cumulants of the diffusion displacement, and the non-Gaussianity of the diffusion propagator can be evaluated via the (excess) diffusional kurtosis, defined by the ratio of the fourth order cumulants to the squared second order cumulants (Jensen et al., 2005). By simply calculating each particle's diffusion displacement $\mathbf{\Delta r} = \boldsymbol{r}(t) - \boldsymbol{r}(0)$ at diffusion time, the diffusivity and the kurtosis along the direction $\hat{n}$ are given by (Fieremans et al., 2008b; Fieremans et al., 2010; Jensen et al., 2005)

$$D(t,\hat{n}) = \frac{\left\langle (\Delta r \cdot \hat{n})^2 \right\rangle}{2t}, \quad \#(2)$$

and

$$K(t,\hat{\mathbf{n}}) = \frac{\left\langle (\Delta \mathbf{r} \cdot \mathbf{n})^4 \right\rangle}{\left\langle (\Delta \mathbf{r} \cdot \hat{\mathbf{n}})^2 \right\rangle^2} - 3, \quad \#(3)$$

respectively.

The diffusion tensor $D_{ij}(t)$ is then estimated by solving

$$D(t,\hat{\mathbf{n}}) = \sum_{ij} D_{ij}(t) n_i n_j$$

via linear least square with $D(t,\hat{n})$ along ≥ 6 non-collinear directions $\hat{n}$ (Basser et al., 1994).

Similarly, the diffusional kurtosis tensor $W_{ijkl}(t)$( ) is estimated by solving

$$D(t,\hat{\mathbf{n}})^2 \cdot K(t,\hat{\mathbf{n}}) = \sum_{ijkl} W_{ijkl}(t) n_i n_j n_k n_l$$

via linear least square with $D(t,\hat{n})$ and $K(t,\hat{n})$ along ≥ 15 non-collinear directions (Jensen et al., 2005).

Once the diffusion tensor $D_{ij}(t)$ is simulated over a wide range of diffusion times for the monopolar pulsed-gradient waveform of a very short gradient pulse width, the apparent diffusivity for any other gradient waveform of low b-value can be calculated

straightforwardly: Based on the Gaussian phase approximation, the apparent diffusivity $\mathrm{ADC} \equiv -\frac{1}{b} \ln S$ is then estimated by (Novikov and Kiselev, 2011)

$$-\ln S \simeq \sum_{ij} \int \mathscr{D}_{ij}(\omega) q_i(\omega) q_j(-\omega) \frac{d\omega}{2\pi}, b \cdot \mathrm{ADC} \ll 1$$

where dispersive diffusivity $\mathscr{D}_{ij}(\omega)$ is the Fourier transform of $\partial_t^2 \left[t D_{ij}(t) \right]$, and $q_i(\omega)$ is the Fourier 11 transform of $\boldsymbol{q}(t)$.

Water exchange—Consider a particle diffusing within a medium of diffusivity D_0, the transmission probability P_{EX} for the particle to pass through a permeable membrane of permeability K is given by (Fieremans et al., 2010; Novikov et al., 2011; Powles et al., 1992; Szafer et al., 1995)

$$P_{\mathrm{EX}} \simeq \frac{\kappa}{D_0} \delta x \cdot C_d, \quad \#(4)$$

where $C_d = 1$ (Powles et al., 1992), $\pi/4$ and 2/3 (Landman et al., 2010; Szafer et al., 1995) for 2 dimensionality 7 = 1, 2, and 3, respectively (see *Appendix A* for derivation). Eq. (4) is applicable only for $P_{EX} \ll 1$ (Fieremans et al., 2010; Powles et al., 1992), yielding the requirement of a small step size:

$$\delta x < \frac{D_0}{\kappa C_d}, \quad \#(5)$$

or effectively $\delta t \ll D_0 / \left(2 d \kappa^2 C_d^2 \right)$ by Eq. (1).

The dimensionality factor uv is sometimes ignored in $1d$ and $3d$ simulations, leading to a discrepancy between the input permeability value and its actual effects in simulations, and has not been considered for 7 $2d$ simulations yet. In this case, the input permeability can be corrected by dividing its value by the 8 dimensionality factor C_d.

Magnetization Transfer (MT): In MT studies so far, “Monte Carlo” simulations usually implied testing the stability of signal models and sampling schemes under different SNR levels (Cercignani and Alexander, 2006; Li et al., 2010; Mougin et al., 2010; Zaiss et al., 2011) by adding Gaussian noise to analytically derived signals, which are effectively simulations of noise propagation rather than MC. In order to achieve actual ab initio MC simulations of MT, similar to exchange, it can be effectively modeled as an “absorbing” membrane, or as a surface relaxation effect. Consider a particle diffusing within a medium of diffusivity D_0, the “absorbing” probability P_{MT} for the particle losing its magnetization by colliding with an absorbing membrane with an effective surface-relaxivity ρ_{eff} is given by (Banavar and Schwartz, 1987; Fieremans et al., 2008a; Sen et al., 1994)

$$P_{\mathrm{MT}} \simeq \frac{\rho_{\mathrm{eff}}}{D_0}\delta x \cdot C_d, \quad \#(6)$$

where uv is the same dimensionality factor in Eq. (4) (see *Appendix B* for the derivation of Eq. (6)). A small step size is required:

$$\delta x \ll \frac{D_0}{\rho_{\mathrm{eff}} C_d}, \quad \#(7)$$

since Eq. (6) only applies to the weak MT effect, i.e. $P_{MT} \ll 1$ (Banavar and Schwartz, 1987; Fieremans et al., 2008a; Sen et al., 1994).

Effective surface relaxation correlates with MT via

$$\rho_{\mathrm{eff}} \equiv \frac{R}{S/V},$$

where R is the MT exchange rate between the liquid pool and the macromolecular pool, and S/V is the surface-to-volume ratio of the microstructure (Baete et al., 2008; Slijkerman and Hofman, 1998), similar to the formula of water exchange (Stanisz, 2003; Stanisz et al., 1997).

Compared with modeling of water exchange (Eq. (4) and Eq. (5)), the modeling of either MT or surface relaxation (Eq. (6) and Eq. (7)) has a very similar functional form since both are derived from the same diffusion equation and similar boundary conditions of the membrane, being absorbing (MT, surface relaxation) versus permeable (water exchange).

IVIM—For a given non-branching capillary geometry with negligible calibers and a well-defined blood flow distribution, IVIM signals can be calculated deterministically without performing any random walk simulations since the step direction is predetermined by the blood flow. A non-branching microvasculature can be created by tracking a random walker moving with (Novikov et al., 2012) or without (Kennan et al., 1994) an inertia toward capillary tree's main direction. MC simulations for the IVIM is necessary only if the capillary tree has complicated geometries, such as branching or nonnegligible diameters in realistic vascular geometries (Gagnon et al., 2015); these cases have not been covered by previous studies of the IVIM, and the gap needs to be filled in the future.

Susceptibility—The off-resonance frequency distribution caused by susceptibility effects is given by (Salomir et al., 2003; Shmueli et al., 2009)

$$\Delta f(\mathbf{r}) = -\frac{\gamma}{2\pi} B_0 \cdot FT^{-1}\left[\left(\frac{1}{3} - \frac{k_z^2}{|\mathbf{k}|^2}\right) \cdot FT(\chi(\mathbf{r}))\right],$$

where B_0 is the main magnetic field, FT is the Fourier transform, k_z is the k-space vector component parallel to B_0, $|\boldsymbol{k}|$ is the magnitude of the k-space vector, and $\chi(\boldsymbol{r})$ is the magnetic susceptibility distribution, manifesting microstructural properties. By accumulating the phase change $d\phi = 2\pi f(\boldsymbol{r}(t))dt$ of each step along each particle's diffusion trajectory $\boldsymbol{r}(t)$ (Weisskoff et al., 1994), the simulated signal of the echo time TE is given by $S(\mathrm{TE}) = \left\langle e^{i\int_0^{\mathrm{TE}} d\varphi} \right\rangle$

T_1 and T_2 relaxation—Consider diffusion simulations of a conventional spin-echo sequence, the signal weighting of T_2 relaxation in each step is $e^{-\delta t/T_2}$ during the echo time (Szafer et al., 1995), where T_2 is the spin-spin relaxation time constant. Similarly, for simulations of a stimulated-echo sequence, the signal weighting of T_2 relaxation during the echo time is the same as for the case of a spin-echo sequence, whereas the signal weighting of T_1 relaxation in each step is $e^{-\delta t/T_1}$ during the mixing time (Woessner, 1961), where T_1, is spin-lattice relaxation time constant. For other sequences, the T_1 and T_2 relaxation effect in each step can be calculated by solving the Bloch-Torrey equation numerically.

3.2 How to set up a Monte Carlo simulation?

Designing the microstructure geometry—To mimic a realistic microstructure geometry, we can arrange, pack and combine multiple simple shapes, in either $2d$ (Fieremans et al., 2010; Hall and Alexander, 2009; Harkins and Does, 2016; Liu et al., 2004) or $3d$ (Balls and Frank, 2009; Budde and Frank, 2010; Ginsburger et al., 2018; Landman et al., 2010; Lin et al., 2016; Palombo et al., 2017; Stanisz et al., 1997; Szafer et al., 1995; Yeh et al., 2013), with a length scale similar to the biological tissue of interest. In gray matter, synaptic boutons and dendritic spines have an average interval of 4.5 μm and 3 μm (Glantz and Lewis, 2000; Hellwig et al., 1994; Shepherd et al., 2002); in WM, the average axonal diameter is ~ 1 μm (Aboitiz et al., 1992; Caminiti et al., 2009; Liewald et al., 2014). For simulations within a porous medium, e.g., restricted diffusion in intra-axonal space of the WM, the packing of isolated pores has no influence on simulation results (Callaghan, 1993). However, for simulations including a non-porous medium, e.g., hindered diffusion in the extra-axonal space of the WM, simulation results depend dramatically on the packing geometry (Fieremans et al., 2008b; Fieremans et al., 2012a; Novikov et al., 2014).

Parallel cylinders packed in a square or a hexagonal lattice (Ford and Hackney, 1997; Lin et al., 2016; Nilsson et al., 2009; Peled, 2007; Sen and Basser, 2005) are common models for highly aligned WM axons. However, histological studies (Aboitiz et al., 1992; Caminiti et al., 2009; Liewald et al., 2014) indicate a random packing geometry for WM axons, which is non-trivial while building a numerical phantom (Burcaw et al., 2015; Fieremans et al., 2008a; Fieremans et al., 2010). It is time-consuming to create a random packing geometry by brute-force methods (Balls and Frank, 2009; Hall and Alexander, 2009), which can be accelerated by placing objects sequentially in descending order of size (Hall et al., 2014), thereby altering the structural disorder making it less randomly packed. Instead, by applying a collision-driven packing generation algorithm (Figure 4, top right) (Donev et al., 2005;

Skoge et al., 2006; Torquato and Jiao, 2010), numerical phantoms can be generated composed of more than thousands of randomly densely packed circles or spheres in any kinds of radius distribution within minutes. Also, an open-source software (AxonPacking) (Mingasson et al., 2017) based on molecular dynamic approaches is available for generating randomly packed circles in Gamma distributed radii and corresponding g-ratio in accordance with histological observations.

The size of a numerical phantom geometry should be much larger than the diffusion length (depending on the total simulated diffusion time t and D_0). If not, simulation results will become sensitive to the specific implementation of the boundary condition.

Particle number—Based on the central limit theorem, MC simulations necessitate including as many particles as possible to achieve an accurate parameter estimation of the ensemble average, i.e. error $\propto 1/\sqrt{\text{particle number}}$. A diffusion simulation without including enough particles effectively lowers the SNR, leading to undesired biases, such as eigenvalue repulsion and overestimated FA for a conventional DTI model (Pierpaoli and Basser, 1996). A clear cut-off for a minimally required number of particles has not been proposed so far, but a rule of thumb often used is that $\geq 10^5$-10^6 particles diffusing from random initial positions generally provide reliable simulation results (Balls and Frank, 2009; Hall and Alexander, 2009; Landman et al., 2010; Yeh et al., 2013), thereby keeping in mind that simulations with a higher degree of freedom (e.g., $3d$ versus $2d$, permeable versus impermeable membranes, hindered versus restricted) require more particles to obtain similar precision.

In general, the recommended particle number is determined by the shape, length scale, and the fieldof-view of the micro-geometry, and is inevitably empirical. As a practical guideline, comparing simulation results (signal, diffusivity and kurtosis) of a simple shape or a collection of simple shapes in a desired field-of-view with their corresponding exact solutions (Section 3.3, *Analytical solutions for timedependent diffusion*, Figure 4, point 3, and *Appendix E*), allows to determine the required particle number (and step size) for simulations in geometries of interest with a length scale similar to the simple shape.

Step size—The step size is limited by the smallest microstructural length scales in a numerical phantom, e.g., for simulations in a geometry composed of parallel randomly packed cylinders, empirically, the minimally required step size was set to be smaller than a tenth of the cylinder radius (Fieremans et al., 2010), or, equivalently, smaller than a tenth of the radius of curvature. In general, accuracy and computational speed of numerical simulations have to balance each other out. To better approach the continuous process of diffusion, simulations with a small step size are required for accurate results, which yet is computationally expensive for a given diffusion time. In contrast, simulations with a large step size facilitate particles to explore a wide region for a given diffusion time and accelerate the computation but also effectively smooth out the contour of the microstructure, i.e. gaining numerical precision in simulated metrics (more particles and/or steps within the same computational time) by losing accuracy.

The time for each step δt, as well as the step size 34 (Eq. (1)), can be limited by the diffusion gradient waveform spectrum. The most commonly used diffusion sequences employ either a pulsed-gradient (PG) or oscillating-gradient (OG) waveform. For MC simulations of PG, δt is limited by the gradient pulse width 3 via a loose constraint: $\delta t \leq \delta$, whereas for OG, δt is limited by the gradient frequency f via $\delta t \ll \frac{1}{f}$. For more complicated diffusion gradient waveforms, δt is limited by the highest frequency $f_{\max}$ of the waveform spectrum via

$$\delta t \ll \frac{1}{f_{\max}}.$$

The above constraint is an approximation of Eq. (C4) (see *Appendix C* for derivations).

For the simulation of water exchange, MT and surface relaxation, Eq. (5) and/or Eq. (7) need to be satisfied as well. So far, no standard criteria for choosing a step size have been raised. Therefore, we will introduce a sanity check in Section 3.3 for choosing an appropriate step size.

Step number—The step number N_{step} is proportional to the diffusion time $t = N_{\text{step}}\ \delta t$. Empirically, the first few thousand steps provide unreliable results, caused by the discretization of a realistic continuous diffusion process into separate steps. This can be evaluated by simulating the kurtosis, which due to discretization, results in $K(t) \sim -1/N_{\text{step}}$ (Lee et al., 2017a). In practice, for the case of free diffusion, $|K(t) - 0| < 0.1\ \%$ implies to include simulation results of $N_{\text{step}} > 1000$, consistent with the suggested step number based on simulations in (Hall and Alexander, 2009). Although it is worthwhile to confirm that the first step of the random walk corresponds to a diffusivity $D(t = \delta t) \simeq D_0$ and a kurtosis $K(t = \delta t) \simeq -2$, $-\frac{3}{2}$ and $-\frac{6}{5}$ for $1d$, $2d$ and $3d$ (see *Appendix D* for the derivation), parameters estimated by the first few thousand steps are often biased and should be discarded in final results.

Boundary condition (substrate edge)—A numerical phantom's finite boundary box, if treated inappropriately, may influence the simulation result. While this edge effect can be diminished at moderate diffusion times by calculating the simulated metrics solely from particles in the central portion of the phantom (Cook et al., 2006), it becomes particularly important at very long diffusion times, during which most of the particles have crossed the box boundaries at least once. To further expand the finite numerical phantom, periodic (Hall and Alexander, 2009) or mirroring (hard wall) boundary conditions are often used.

For a periodic boundary condition, the numerical phantom is repeated by the same copy of itself (Hall and Alexander, 2009). When a particle hits a boundary, it goes through the boundary box face and comes back from the other side of the boundary box; the number of jumps from one side of the box to another is recorded. This approach is particularly well suited for packing geometries that have no microstructural objects touching the box boundaries, or have a periodicity in the packing that matches the matrix size. However, geometrical discontinuities over the boundary, if not treated properly while building the

phantom, could introduce additional “restricted” diffusion effect corresponding to the box size.

Alternatively, for a mirroring boundary condition, the numerical phantom is repeated by its reflective copies. Particle’s initial positions are swapped with respect to the box face the particle is crossing to mimic the diffusion out of the boundary box. The effective repetition unit of the phantom geometry is 2^d larger than the original phantom. Although mirroring may result in increased fiber orientation dispersion, e.g., in the case of a straight fiber along the diagonal of a box, this replication method prevents microstructural discontinuity over the boundary.

Impermeable, permeable and absorbing membranes: If a particle encounters an impermeable membrane within a step, the particle is reflected back by the membrane and experiences a perfectly elastic collision (Hall and Alexander, 2009; Szafer et al., 1995). The displacements before and after the collision are then summed up to the step size given by Eq. (1).

While encountering a permeable membrane, the particle has a probability $1-P_{\mathrm{EX}}$ (Eq. (4)) to be reflected elastically by the membrane, and a probability P_{EX} to penetrate through. Considering a particle in compartment 1 crossing a membrane and entering compartment 2, if the particle walks $v\cdot\delta x_1$, in compartment 1 ($0\leq v\leq 1$), the particle will walk $(1-v)\cdot\delta x_2$ along the same direction in compartment 2, where δx_1, and δx_2 are the step size in compartments 1 and 2 without hitting any membrane (Szafer et 1995). Also, the total $T2$-weighting of the step is $e^{-v\cdot\delta t/T_2^{(1)}}\cdot e^{-(1-v)\cdot\delta t/T_2^{(2)}}$, where $T_2^{(1)}$ and $T_2^{(2)}$ are T_2 relaxation time constants in compartments 1 and 2 (Szafer et al., 1995). Adjustment of the step size is crucial for maintaining the particle-density balance between different compartments when simulating water exchange.

Similarly, but differently, while encountering an absorbing membrane, the particle has a probability $1-P_{\mathrm{MT}}$ (Eq. (6)) to be elastically reflected, and a probability xy to lose its magnetization completely, effectively being “absorbed” by the membrane.

Particle-membrane interaction: elastic collision (specular reflection), diffuse reflection, and equal-step-length random leap—In the field of diffusional MC simulations, the most commonly implemented particle-membrane interaction is elastic collision (specular reflection) (Hall and Alexander, 2009), which works quite well not just for impermeable membranes but also for permeable and/or absorbing membranes. It is worthwhile to notice that having more than one elastic collision within a step is possible, especially in a densely packed geometry.

Other kinds of particle-membrane interaction include diffuse reflection (Baete et al., 2008; Xing et al., 2013) and equal-step-length random leap (Xing et al., 2013). For diffuse reflection (Baete et al., 2008; Xing et al., 2013), the particle reflected by a membrane consumes the rest of its step length in a random direction over the same side of the membrane. For equal-step-length random leap (Xing et al., 2013), the particle encountering

a membrane cancels the original step and randomly chooses another direction to leap until the chosen step does not cross any membranes. When the step number is sufficiently large and the step size is reasonable small (compared with the length scale in the microstructure), the two nonelastic interactions results agree with results from elastic collision with impermeable membranes (Xing et al., 2013), though this has not been tested for permeable and absorbing membranes.

Relieving the computational bottleneck: For simulations within a medium composed of multiple compartments, the most computationally expensive calculation is to identify which compartment a particle resides in at a given time. Despite advances in computational resources including the use of clusters and GPUs, checking against all compartments at each step is inefficient and should be avoided. A way to solve this problem is to build a lookup table (Hall et al., 2014; Yeh et al., 2013): By partitioning the numerical phantom into multiple cassettes, the lookup table records labels of compartments, partially or completely included within each cassette (Figure 4, top right). When a particle diffuses across several cassettes in a step, we only need to check compartments labeled by those cassettes. Such algorithm reduces the search to a local sub-volume scale and thereby significantly speeds up simulation run times.

3.3 How to proof check your Monte Carlo simulation framework?

Before performing a MC simulation to validate a tissue model, it is helpful to verify the numerical implementation by comparing against well-known solutions. In particular, following criteria can be used to perform quality control. (The detail of suggested simulation examples shown in Figure 4 is provided as *Supplementary Information*.)

Free diffusion—In the case of free diffusion, both diffusivity and kurtosis display no time-dependence, yielding a simulated diffusivity, $D(t) \simeq D_0$, and kurtosis, $|K(t)| \ll 1$. Since, theoretically, the kurtosis of the first few steps are negative (Section 3.2 *step number*), the step number corresponding to a near-zero kurtosis serves as a reference to discard simulation results of early steps. Furthermore, the diffusivity $D(t=\delta t)$ and kurtosis $K(t=\delta t)$ of the first step, mentioned in Section 3.2 *step number*, indicate the randomness of the assigned step orientation. Examples of free diffusion include diffusion parallel to planes and along cylindrical axes. For a reliable simulation result, the error of diffusivity and kurtosis, defined by $\left|\frac{D(t)}{D_0} - 1\right|$, should be very small ($< 10^{-2}$ - 10^{-3}) at diffusion time (Figure 4, point 1).

Diffusion time dependence in short-time limit (S/V limit)—When the diffusion time is so short that only particles around restrictions (e.g., cell membrane, myelin sheath) have a chance to encounter them, the time-dependent D (Mitra et al., 1993; Novikov et al., 2009; Novikov et al., 2011) and K (Jensen and Helpern, 2010; Novikov et al., 2009) are given by

$$D(t) \simeq D_0\left[1 - \frac{S}{Vd}\left(\frac{4\sqrt{D_0 t}}{3\sqrt{\pi}} - \kappa t\right)\right], \quad \#(8a)$$

$$K(t) \simeq \frac{S}{V}\beta_d\left[\frac{8\sqrt{D_0 t}}{5\sqrt{\pi}} - 2\kappa t\right], \quad \#(8b)$$

where $\beta_d = \langle \cos^4 \theta \rangle = 1$, 3/8 and 1/5 in $1d$, $2d$ and $3d$, and S/V is the surface-to-volume ratio of the studied geometry. The diffusion time-dependence in short-time limit is universal, and valid for systems consisting of permeable/impermeable membranes and applicable to any kind of micro-geometries (Figure 4, point 2). Failing to match simulation results with Eq. (8) may indicate an error related to the implementation of elastic collisions.

Analytical solutions for time-dependent diffusion—Performing simulations in specific simple shapes is a common way to verify simulation implementations and determine the required particle number and step size. Callaghan derived exact solutions of dMRI signals for parallel planes, cylinders and spheres with impermeable (non-) absorbing membranes (Callaghan, 1995). Based on Callaghan's work, we further derived analytical solutions in *Appendix E* for the time-dependent diffusivity (Burcaw et al., 2015; Callaghan, 1993) and kurtosis in these shapes. In particular, for periodic parallel planes of permeable membranes, Novikov et al. derived the analytical solution of the instantaneous diffusivity $D_{\text{inst}} \equiv \frac{1}{2}\partial_t x^2$, eq. [S25] in (Novikov et al., 2014).

Particle density balance for the water exchange—For random walk simulations across permeable membranes, it is important to ensure that average particle densities in each compartment are almost the same, i.e. < 0.1–1 % differences between compartments, when a homogeneous particle density is initialized across all compartments. Failing to maintain a homogeneous particle density throughout different compartments potentially biases any simulated metric. For example, consider a toy model composed of two pools, i.e. a fast pool (high diffusivity) and a slow pool (low diffusivity), separated by a permeable membrane. This toy model is a simplified model for WM simulations (intra-/extra-axonal water (fast pool) and myelin water (slow pool)). If the particle density in slow pool is higher than that in fast pool, the simulated ADC as well as the signal change will be overrepresented by the slow pool and thus be underestimated; also, the simulated kurtosis will be biased and approach to a non-zero constant at long diffusion times.

A particle density imbalance implies an error to implement elastic collisions and membrane permeation. Furthermore, to ensure that simulation results are consistent to input membrane properties, such as (effective) surface-relaxivity ρ and permeability k, the temporal evolution of particle densities a(x) around the membrane can be studied (Figure 4, point 5). For that, consider a $1d$ diffusion simulation on the right side of a single absorbing membrane positioned at x_M, where the particle density around the membrane (x_M^+ on the right side) satisfies (Callaghan, 1995)

$$-D_0 \cdot \left|\partial_x n\left(x_M^+\right)\right| + \rho \cdot n\left(x_M^+\right) = 0, \quad \#(9)$$

or equivalently $\rho = D_0 \cdot \left|\partial_x n\left(x_M^+\right)\right| / n\left(x_M^+\right)$. Similarly, for a $1d$ diffusion simulation of a single permeable membrane positioned at x_M, the particle density around the membrane (x_M^+ on the right side and x_M^- on the left side) obeys (Powles et al., 1992)

$$-D_0^+ \cdot \partial_x n\left(x_M^+\right) = -D_0^- \cdot \partial_x n\left(x_M^-\right) = \kappa \cdot \left[n\left(x_M^-\right) - n\left(x_M^+\right)\right], \quad \#(10)$$

where D_0^+ and D_0^- are diffusivities on the right and the left side of the membrane. Also, Eq. (9) and Eq. (10) are applicable to $2d$ (Figure 4, point 5) and $3d$ cases. Inconsistencies between the input and estimated values by Eq. (9) and Eq. (10) indicate errors in implementing elastic collisions or a missing dimensionality factor uv in Eq.(4) and Eq. (6). Although Eq. (9) and Eq. (10) are theoretically applicable for membranes of all shapes, they work particularly well for locally flat membranes in actual implementations since the step size needs to be much smaller than the local membrane curvature (Section 3.2, *Step size*), equivalent to the condition of locally flat membranes.

3.4 Examples

Random walk MC simulations have been widely used to validate microstructural modeling of neural tissues particular for diffusion, as also reviewed in (Jelescu and Budde, 2017; Zhang, 2016), and illustrated in Figure 5. To date, several open source software tools for numerical simulations focusing on diffusion exist, including the most widely used Camino (Hall and Alexander, 2009), DW-MRI Random Walk Simulator (Landman et al., 2010), DIFSIM (Balls and Frank, 2009; Baxter and Frank, 2013), and Diffusion Microscopist Simulator (Yeh et al., 2013), some works using those are included in the overview below.

Simulations of water exchange and its effect of diffusion on biophysical modeling were attempted first, for regularly packed cuboid cells (Szafer et al., 1995), square tubes (Stanisz et al., 1997) and circular cylinders (Ford and Hackney, 1997) of the same size. In particular, the applicability of the Kärger model was tested in hexagonally packed (Nilsson et al., 2010) and randomly packed cylinders (Fieremans et al., 2010). Besides two compartmental systems (mimicking intra- and extra-axonal space), water exchange between multiple compartments was also simulated more recently, either by adding an extra component of glial cells (Lin et al., 2016) or myelin sheaths of finite thickness with (Lin et al., 2018) or without (Harkins and Does, 2016) considering T_2 differences between myelin sheaths and other compartments.

In WM, MC simulations of diffusion have been shown useful for investigating relevant axonal features, and determining length scales in the intra-axonal space, in order to validate inner axon diameter mapping (Alexander et al., 2010). Furthermore, the axonal shape was modeled and simulated to account for physiological and pathological changes potentially detectable by dMRI, e.g., due to neurite beading (Budde and Frank, 2010; Ginsburger et al., 2018), the presence of nodes of Ranvier (Ginsburger et al., 2018), and axonal undulation (Ginsburger et al., 2018; Nilsson et al., 2012). Furthermore, the accuracy and robustness of

tractography algorithms in crossing-fiber regions was evaluated using simulations (Poupon et al., 2008; Ramirez-Manzanares et al., 2011; Yeh et al., 2013).

Diffusion simulations have been shown particularly useful to assess the effect of the axon packing geometry in the long time (tortuosity) limit, for which theory development is an active topic of research (Fieremans et al., 2012a). The effect of varying axonal water fraction on diffusion metrics was explored by simulating the fractional anisotropy (Stikov et al., 2011) and tortuosity of the extra-axonal space, in addition to modeling demyelination versus axonal loss (Fieremans et al., 2008b; Fieremans et al., 2012a).

Diffusion simulations have also been used to validate models for time-dependent diffusion. The applicability of estimating surface-to-volume ratio via oscillating gradients was evaluated by simulations of either fibers (Schachter et al., 2000) or synthetic substrates mimicking dendritic spines (Palombo et al., 2017). Simulations in densely packed fiber geometries were performed to explore frequency-dependence (Lam et al., 2015), as well as time-dependence of diffusion in the extra-axonal space (Burcaw et al., 2015; De Santis et al., 2016; Fieremans et al., 2008b; Novikov and Kiselev, 2010).

While so far mostly done to model diffusion in dedicated microgeometries, MC simulations have also been used to evaluate the influence of diffusion on the contrast caused by local field inhomogeneities, such as with blood-oxygenation-level-dependent contrast either in simplified geometries (Boxerman et al., 1995) or in realistic vascular structures (Gagnon et al., 2015) and mesoscopic susceptibility effect (Laun et al., 2009; Ruh et al., 2018; Weisskoff et al., 1994; Xu et al., 2018).

4. Discussion

Numerous phantoms have been proposed for the validation of microstructural mapping, both physical (hardware) and numerical (software). Physical phantoms, in general, are useful to verify both the precision and accuracy of imaging methods (Keenan et al.). Microstructural phantoms, i.e. those exhibiting features over micrometer length scales along with the requirements described in Section 2.1, are often challenging to manufacture in a reproducible way and therefore typically not used to evaluate precision, e.g., in multicenter trials. Instead, they are essential for evaluating the accuracy of several microstructural contrast mechanisms by providing a ground-truth to compare biophysical models against. Similarly, software phantoms (based on MC) are instrumental for evaluating accuracy of theoretical models, and gaining better understanding of experimental effects.

When reviewing the literature on physical phantoms for testing and validating microstructural MRI phantoms, it became clear that most true microstructural phantoms proposed so far are for evaluating dMRI, and to a lesser extent for IVIM. In particular, there is an abundancy of phantoms proposed to mimic diffusion in brain WM (Table 2, Figure 2), either using capillaries with an I.D. ranging 1 – 50 μm to model diffusion in the intra-axonal space, or plain fibers with an O.D. of 10 – 20 μm to model diffusion in the extra-axonal space. Most recently, biomimetic phantoms made of hollow fibers (I.D. 12 μm, O.D. 34 μm), dubbed as ‘taxons’, have been proposed that could model to some extent both diffusion in

the intra- and extra-axonal space simultaneously. While these phantoms are quite popular for evaluating fiber tracking and performing quality control, they have also been insightful for directly validating biophysical models, e.g., for pore size (‘axon diameter’) and compartment fraction (‘neurite density’) mapping methods, and time-dependent diffusion in the extra-axonal space (see Table 2 for references). On the other hand, no gray matter phantoms have been suggested, with the exception of (Komlosh et al., 2007) proposing a packing of randomly oriented glass capillaries filled with water and immersed in deuterated 1,2-di-chloro-benzene, such that the proton signal only comes from inside the tubes. Altogether, the need for more realistic physical phantoms for brain microstructure remains, e.g., to model gray matter, axonal dispersion and undulations, permeability, as well as different types of pathology, e.g., axonal beading, demyelination, etc.

Far less microstructural phantoms have been proposed so far to study other microstructural imaging contrasts including MT or susceptibility imaging. One interesting future direction would be to develop a universal phantom that has well-characterized properties in terms of dimensions, MT effects (including surface relaxation) and magnetic susceptibility values, ideally similar to the brain. So far, few examples exist of phantoms that have been characterized in term of several microstructural contrasts, including dairy cream for T_2 relaxation and diffusion, or cross-linked dextran gel (sephadex™) for diffusion, susceptibility and IVIM, but none have been fully characterized so far. Ultimately, full characterization would enable to fully understand the behavior of such multimodal phantom.

While physical phantoms are ultimately attractive because of their well-known specs and their potential for standardization, on the other hand, they are somewhat limited for the validation of microstructural methods as they fail to capture the microstructural complexity of the brain in healthy state, and even more so, in pathological state. Instead, biological phantoms, either using unfixed (Schmierer et al., 2007), or fixed brain tissue (Dyrby et al., 2013; Shepherd et al., 2009a; West et al., 2018) as well as viable tissue (Blackband et al., 1997; Richardson et al., 2013) have the microstructure that is more similar to the *in vivo* brain, and are discussed in detail elsewhere in this Special Issue. On the downside, biological tissue is not widely available, and the preparation requires specialized knowledge (Shepherd et al., 2009a; Shepherd et al., 2009b). Their exact structure remains in general unclear and they are not suitable for calibration purposes due to their limited storage time and lack of stability.

Numerical phantoms offer an appealing alternative, as they are very flexible and can be sophisticated to model the brain microstructure very realistically in terms of different microstructural effects and substrates. So far, most of the diffusion simulation studies, including non-MC studies, are implemented in geometries containing artificial geometrical shapes. Benefitting from recent advances in histology analysis techniques (Schindelin et al., 2012), makes it possible now to perform simulations in realistic microstructure reconstructed from microscopy images of neural tissues (Chin et al., 2002; Xu et al., 2018). These attempts are hitherto limited to $2d$ simulations (Figure 5), except for limited $3d$ simulations in foam (Baete et al., 2008) and asparagus (Panagiotaki et al., 2010), and prompt for more extensive $3d$ simulation studies in realistic micro-geometries of neuronal tissues.

While biophysical models are typically validated by either physical or numerical phantoms, few studies so far used both of them (Burcaw et al., 2015; Fieremans et al., 2008a; Fieremans et al., 2008b; Gagnon et al., 2015; Laun et al., 2009; Poupon et al., 2008; Schachter et al., 2000; Weisskoff et al., 1994)). Indeed, additional insight could be gained by combining physical phantoms with numerical simulations. The most comprehensive validation of targeted models can be done by building a numerical phantom based on characterization of a physical phantom (e.g., by performing micro-CT (Fieremans et al., 2008b), or SEM (Fan et al., 2018)), and comparing physical phantom experiment with numerical simulation. Again here, understanding all factors affecting the microstructural MR contrasts both experimentally and in simulations are essential to understand the phantom's behavior, thereby ultimately creating a universal multimodal microstructural (hardware and software) phantom.

5. Conclusion

Phantoms, both numerical and physical, offer the perspective of providing a ground-truth useful to validate microstructural imaging methods, a critical and necessary step to enable microstructural quantification in neuronal development and disorders. Physical microstructural phantoms consist of (NMR invisible) materials immersed in an (NMR visible) liquid, whereby the characteristics of both components determine the microstructural properties measured with MRI. Microfibers, either hollow or plain, along with capillaries have been frequently used to mimic brain microstructure. Numerical microstructural phantoms are particularly appealing because of their great flexibility in microstructural substrates and modeling of different biophysical mechanisms. While many phantoms exist already, the current review also aims to stimulate further research in the field, to obtain well-characterized physical phantoms closely mimicking brain's microstructure, and optimal numerical simulations that can be performed in realistic microstructures and include the multitude of biophysical mechanisms underlying the MR contrast in microstructural imaging.

Supplementary Material

Refer to Web version on PubMed Central for supplementary material.

Acknowledgments

We would like to thank Michael Boss, Matthew Cronin, Richard Dortch, Marios Georgiadis, Martijn Kloos, Chunlei Liu, Dmitry Novikov, Eric Sigmund, Greg Stanisz, and Nicole Wake for fruitful discussions generating input for this manuscript, Steven Baete for providing Figure 3c. This study was supported in part by grants R01 NS088040 and R01 NS039135–11 from the NINDS (NIH), and by the Center of Advanced Imaging Innovation and Research (CAI2R, www.cai2r.net), a NIBIB Biomedical Technology Resource Center: P41 EB017183.

Appendix A.: Dimensionality factor ¸Cd in Eq. (4)

The original version of Eq. (4) for the transmission probability in (Fieremans et al., 2010; Powles et al., 1992) is

$$P'_{\mathrm{EX}} \simeq \frac{2\kappa \cdot \delta s}{D_0}, \quad \#(A1)$$

where $\delta s \leq \delta x$ is the distance between the particle and the membrane. By approximating δs with δx, which is equivalent to taking the average $\langle \delta s \rangle$ over the region around the membrane, an unknown constant C_d is introduced in Eq. (4).

Considering a compartment containing Np particles, the particle number change δN_p, from losing particles due to exchange, is

$$\delta N_P \simeq \left(\frac{N_P}{V}\right) \cdot (S \cdot \delta x) \cdot p_\Omega \cdot P_{\mathrm{EX}}, \quad \#(A2)$$

where V is the volume of the compartment, S is the surface area of the membrane covering the compartment, an p_Ω is the fraction of the hopping orientation along which particles encounter the membrane. By substituting Eq. (1) and Eq. (4) into Eq. (A2), the change rate of the particle number is

$$\frac{\delta N_P}{\delta t} = \left(\kappa \frac{S}{V}\right) \cdot N_P \cdot \left(p_\Omega \cdot C_d \cdot 2d\right). \quad \#(A3)$$

The Bloch-Torrey equation for water exchange is given by

$$\frac{\delta N_P}{\delta t} = k_{\mathrm{EX}} \cdot N_P, \quad \#(A4a)$$

$$k_{\mathrm{EX}} = \kappa \frac{S}{V}, \quad \#(A4b)$$

where k_{EX} is the exchange rate (Stanisz, 2003; Stanisz et al., 1997). Comparing Eq. (A3) and Eq. (A4), (p_Ω, C_d $2d$)=1 needs to be satisfied, leading to

$$C_d = \left(p_\Omega \cdot 2d\right)^{-1}. \quad \#(A5)$$

For $1d$ case (Figure A1a), the calculation of $p_\Omega = \frac{1}{1+1} = \frac{1}{2}$ is trivial. For $2d$ case (Figure A1b), averaging ¼½ over the area surrounding the membrane with a thickness 34, we obtain

$$p_{\Omega} = \frac{1}{\delta x}\int_0^{\delta x} \frac{2\cos^{-1}(\delta s/\delta x)}{2\pi} d(\delta s) = \frac{1}{\pi}.$$

Similarly, for p_{Ω} case (Figure A1c), averaging p_{Ω} over the volume surrounding the membrane with a 2 thickness δx, we have

$$p_{\Omega} = \frac{1}{\delta x}\int_0^{\delta x} \frac{1}{2}\left(1 - \frac{\delta s}{\delta x}\right) d(\delta s) = \frac{1}{4}.$$

Substituting p_{Ω} into Eq. (A5), we obtain the dimensionality factor C_d in Eq. (4).

Appendix B.: "Absorbing" probability of MT and surface relaxation in Eq. (6)

Here we adopt a similar approach as in (Fieremans et al., 2010; Powles et al., 1992) to derive Eq. (A1), referring to fig. 7 in (Fieremans et al., 2010): Considering a $1d$ case, where an "absorbing" membrane is positioned at x_m and the substrate diffusivity is 8, the probability of a particle showing at position 4& on the right side of the membrane at time $t + \delta t$, such that $x_p - x_{\mathrm{M}\pm} < \delta x$, is related to the probabilities of previous steps at time t by

$$\mathscr{P}(x_P, t+\delta t) = \frac{1}{2}\mathscr{P}(x_P + \delta x, t) + 0 \cdot \frac{P_{\mathrm{MT}}}{2}\mathscr{P}(x_P - \delta x, t) + \frac{1 - P_{\mathrm{MT}}}{2}\mathscr{P}(2x_M - x_P + \delta x, t),$$

#(B1)

where $\mathscr{P}(\cdot)$ is the probability density function (PDF) of the particle population at a given position and time, and the second term is "absorbed" by the membrane, c.f. eq. [40] in Ref (Fieremans et al., 2010).

The PDF $\mathscr{P}(\cdot)$ obeys the diffusion equation

$$\partial_x^2 \mathscr{P} = \partial_t \mathscr{P}. \quad \#(B2)$$

The boundary condition of the absorbing membrane with an effective surface-relaxivity ρ_{eff} is (Callaghan, 1995)

$$-D_0 \partial_x \mathscr{P} + \rho_{\mathrm{eff}} \mathscr{P} = 0. \quad \#(B3)$$

Expanding each term in Eq. (B1) by Taylor series around $x = x_M$, substituting Eq. (B2) and Eq. (B3) into Eq. (B1), and ignoring higher order terms, we obtain, for weak MT and surface relaxation $\left(\frac{\delta x_{-}\rho_{\text{eff}}}{D_0} \ll 1\right)$,

$$P_{\text{MT}} \simeq \frac{2\delta x_{-}\rho_{\text{eff}}}{D_0}, \quad \#(\text{B4})$$

where $\delta x_{-} = \delta x + x_M - x_p$ is the distance between the particle and the membrane before the particle is encountering and being absorbed by the membrane, corresponding to the second absorbed term in Eq. (B1).

Eq. (B4) is very similar to Eq. (A1). It is then straightforward to derive Eq. (6) by including the dimensionality factor discussed in *Appendix A*.

Appendix C.: The highest frequency of the diffusion gradient waveform spectrum limits the time of each step

Consider a $1d$ simulation, a time-varying diffusion gradient $g(t)$ within a step can be approximated by its Taylor expansion at time $t=t_0$:

$$g(t) \simeq g_0 + \left(\partial_t g_0\right)\cdot\left(t - t_0\right) + \frac{1}{2!}\left(\partial_t^2 g_0\right)\cdot\left(t - t_0\right)^2 + \frac{1}{3!}\left(\partial_t^3 g_0\right)\cdot\left(t - t_0\right)^3, \quad \#(\text{C1})$$

where $g_0 = g(t_0)$ is the diffusion gradient at $t = t_0$, and $\partial_t g_0$, $\partial_t^2 g_0$ and $\partial_t^3 g_0$ are the corresponding first, second and third order derivatives with respect to time. Supposing that a particle's position $x(t) \simeq x(t_0) \equiv x_0$ is almost the same within a step, the diffusion phase $\delta\varphi$ induced during the step is given by

$$\delta\varphi = \int_{t_0 - \frac{1}{2}\delta t}^{t_0 + \frac{1}{2}\delta t} \gamma g(t)\cdot x_0 dt\,. \quad \#(\text{C2})$$

Substituting Eq. (C1) into Eq. (C2), we obtain

$$\delta\varphi \simeq \gamma g_0 x_0\cdot(\delta t) + \frac{1}{24}\gamma\left(\partial_t^2 g_0\right)x_0\cdot(\delta t)^3, \quad \#(\text{C3})$$

where the first term of RHS is the expected diffusion phase, and the second term of RHS is the unwanted bias caused by diffusion gradient's temporal variations; when the bias is negligible, i.e. the second term is much smaller than the first term, the following condition is satisfied:

$$\delta t \ll \sqrt{\left|\frac{24 g_0}{\partial_t^2 g_0}\right|}. \quad \#(C4)$$

For a pulsed-gradient waveform, Eq. (C4) provides no constraints as long as 3 is no bigger than the gradient pulse width. For an oscillating-gradient waveform $g(t) \propto \cos 2\pi f t$ of the frequency f, Eq. (C4) degenerates to $\delta t \ll \frac{\sqrt{24}}{2\pi f} \sim \frac{1}{f}$. For the general case, by applying Fourier transforms to diffusion gradient waveforms, Eq. (C4) approximates to $\delta t < \frac{\sqrt{24}}{2\pi f_{\max}} \sim \frac{1}{f_{\max}}$.

Appendix D.: Kurtosis at the first step

Given that all particles only make one step with a step size δx in Eq. (1), the kurtosis in $1d$, based on Eq. (3), is given by

$$K(t = \delta t) = \frac{\delta x^4}{\left(\delta x^2\right)^2} - 3 = -2$$

For the $2d$ case, given that Θ is the angle between $\mathbf{\Delta r}$ and $\hat{n}$ in Eq. (3), the kurtosis is calculated by

$$K(t = \delta t) = \frac{\frac{1}{2\pi}\int_0^{2\pi} \cos^4\theta d\theta}{\left(\frac{1}{2\pi}\int_0^{2\pi} \cos^2\theta d\theta\right)^2} - 3 = -\frac{3}{2}.$$

Similarly, the kurtosis in $3d$ is given by

$$K(t = \delta t) = \frac{\frac{1}{2}\int_0^{\pi} \cos^4\theta \cdot \sin\theta d\theta}{\left(\frac{1}{2}\int_0^{\pi} \cos^2\theta \cdot \sin\theta d\theta\right)^2} - 3 = -\frac{6}{5}.$$

Appendix E.: Analytical solutions for the diffusion time-dependence in specific geometries

Consider the diffusion within a pore bounded by an impermeable membrane with surface-relaxivity ρ, the analytical form of dMRI signals is known for some specific shapes, such as parallel planes, cylinders and spheres (Callaghan, 1995). Expanding solutions of the dMRI signals using Taylor series with respect to qa, where q is the Fourier domain of diffusion displacements and a is the pore size, we then can derive the time-dependent diffusivity and kurtosis as follows.

For diffusion between **parallel planes** of impermeable membranes (with given surface-relaxivity ρ), with spacing $2a$, the diffusivity and kurtosis are given by

$$D(t) = \frac{a^2}{t}\left(\frac{1}{3} - \sum_{m=0}^{\infty} \frac{2}{\zeta_m^4} e^{-\zeta_m^2 \frac{t}{t_c}}\right)$$

$$K(t) = \frac{6}{[D(t)]^2} \cdot \left[\frac{2}{45} + \sum_{n=1}^{\infty} \frac{2}{\xi_n^4} e^{-\xi_n^2 \cdot \frac{t}{t_c}} + \sum_{m=0}^{\infty} \frac{2}{\zeta_m^4}\left(-1 + \frac{2}{\zeta_m^2}\right) e^{-\zeta_m^2 \cdot \frac{t}{t_c}}\right] - 3,$$

where ξ_n and ς_m are the roots of $\xi_n \cdot \tan \xi_n = \rho a / D_0$ and $\zeta_m \cdot \cot \zeta = -\rho a / D_0$ (Callaghan, 1995), and $t_c = a^2/D_0$ is the correlation time, i.e. the average time for particles to diffuse between restrictions. For non-absorbing membranes, $\rho = 0$.

For diffusion **within a cylinder** of radius ¨, bounded by impermeable membranes (surface-relaxivity), the diffusivity (Burcaw et al., 2015) and kurtosis are given by

$$D(t) = \frac{a^2}{t}\left[\frac{1}{4} - \sum_{k=1}^{\infty} \frac{2}{\beta_{1k}^2\left(\beta_{1k}^2 - 1\right)} e^{-\beta_{1k}^2 \cdot \frac{t}{t_c}}\right],$$

$$K(t) = \frac{6}{[D(t)]^2} \cdot [\frac{5}{192} + \sum_{k=2}^{\infty} \frac{1}{\beta_{0k}^4} e^{-\beta_{0k}^2 \frac{t}{t_c}} + \sum_{k=1}^{\infty} \frac{4}{\beta_{1k}^2\left(\beta_{1k}^2 - 1\right)}\left(\frac{1}{\beta_{1k}^2} - \frac{3}{8}\right) e^{-\beta_{1k}^2 \frac{t}{t_c}}$$
$$+ \sum_{k=2}^{\infty} \frac{1}{2\beta_{2k}^2\left(\beta_{2k}^2 - 4\right)} e^{-\beta_{2k}^2 \frac{t}{t_c}}] - 3,$$

where β_{nk} is the root of $\beta_{nk} \cdot J_n'(\beta_{nk}) / J_n(\beta_{nk}) = -\rho a / D_0$ (Callaghan, 1995), $J_n(\cdot)$ is the Bessel function, and $t_c = a^2/D_0$ is the correlation time.

For diffusion **within a sphere** of radius ¨, bounded by impermeable membranes (surface-relaxivity), the diffusivity and kurtosis are given by

$$D(t) = \frac{a^2}{t}\left[\frac{1}{5} - \sum_{k=1}^{\infty} \frac{2}{\alpha_{1k}^2\left(\alpha_{1k}^2 - 2\right)} e^{-\alpha_{1k}^2 \frac{t}{t_c}}\right],$$

$$K(t) = \frac{6}{[D(t)]^2} \cdot [\frac{3}{175} + \sum_{k=2}^{\infty} \frac{2}{3\alpha_{0k}^4} \cdot e^{-\alpha_{0k}^2 \frac{t}{t_c}} + \sum_{k=1}^{\infty} \frac{4}{\alpha_{1k}^2\left(\alpha_{1k}^2 - 2\right)}\left(\frac{1}{\alpha_{1k}^2} - \frac{3}{10}\right)e^{-\alpha_{1k}^2 \frac{t}{t_c}} + \sum_{k=2}^{\infty} \frac{8}{15\alpha_{2k}^2\left(\alpha_{2k}^2 - 6\right)} e^{-\alpha_{2k}^2 \frac{t}{t_c}}] - 3,$$

where α_{nk} is the root of $\alpha_{nk} \cdot j_n'(\alpha_{nk})/j_n(\alpha_{nk}) = -\rho a/D_0$ (Callaghan, 1995), $J_n(\cdot)$ is the spherical 11 Bessel function, and $t_c = a^2/D_0$ is the correlation time.

References

Ababneh Z, Haque M, Maier SE, Mulkern RV, 2004 Dairy cream as a phantom material for biexponential diffusion decay. Magnetic Resonance Materials in Physics, Biology and Medicine 17, 95100.

Aboitiz F, Scheibel A, Fisher R, Zaidel E, 1992 Fiber composition of the human corpus callosum. Brain Research 598, 143–153. [PubMed: 1486477]

Alexander DC, Hubbard PL, Hall MG, Moore EA, Ptito M, Parker GJ, Dyrby TB, 2010 Orientationally invariant indices of axon diameter and density from diffusion MRI. NeuroImage 52, 1374–1389. [PubMed: 20580932]

Anscombe N, 2010 Direct laser writing. Nat Photon 4, 22–23.

Åslund I, Nowacka A, Nilsson M, Topgaard D, 2009 Filter-exchange PGSE NMR determination of cell membrane permeability. Journal of Magnetic Resonance 200, 291–295. [PubMed: 19647458]

Åslund I, Topgaard D, 2009 Determination of the self-diffusion coefficient of intracellular water using PGSE NMR with variable gradient pulse length. Journal of Magnetic Resonance 201, 250–254. [PubMed: 19800273]

Avram L, Assaf Y, Cohen Y, 2004 The effect of rotational angle and experimental parameters on the diffraction patterns and micro-structural information obtained from q-space diffusion NMR: implication for diffusion in white matter fibers. Journal of Magnetic Resonance 169, 30–38. [PubMed: 15183354]

Baete SH, Cho G, Sigmund EE, 2013 Multiple-echo diffusion tensor acquisition technique (MEDITATE) on a 3T clinical scanner. NMR in Biomedicine 26, 1471–1483. [PubMed: 23828606]

Baete SH, De Deene Y, Masschaele B, De Neve W, 2008 Microstructural analysis of foam by use of NMR R2 dispersion. J Magn Reson 193, 286–296. [PubMed: 18534878]

Balls GT, Frank LR, 2009 A simulation environment for diffusion weighted MR experiments in complex media. Magn Reson Med 62, 771–778. [PubMed: 19488991]

Banavar JR, Schwartz LM, 1987 Magnetic resonance as a probe of permeability in porous media. Physical Review Letters 58, 1411–1414. [PubMed: 10034429]

Bar-Shir A, Avram L, Ozarslan E, Basser PJ, Cohen Y, 2008 The effect of the diffusion time and pulse gradient duration ratio on the diffraction pattern and the structural information estimated from qspace diffusion MR: experiments and simulations. J Magn Reson 194, 230–236. [PubMed: 18667345]

Basser PJ, Mattiello J, LeBihan D, 1994 Estimation of the effective self-diffusion tensor from the NMR spin echo. J Magn Reson B 103, 247–254. [PubMed: 8019776]

Baxter GT, Frank LR, 2013 A computational model for diffusion weighted imaging of myelinated white matter. NeuroImage 75, 204–212. [PubMed: 23507381]

Beltrachini L, Taylor ZA, Frangi AF, 2015 A parametric finite element solution of the generalised Bloch-Torrey equation for arbitrary domains. J Magn Reson 259, 126–134. [PubMed: 26334960]

Benjamini D, Komlosh ME, Basser PJ, Nevo U, 2014 Nonparametric pore size distribution using d-PFG: Comparison to s-PFG and migration to MRI. Journal of Magnetic Resonance 246, 36–45. [PubMed: 25064269]

Bieniosek MF, Lee BJ, Levin CS, 2015 Technical Note: Characterization of custom 3D printed multimodality imaging phantoms. Medical Physics 42, 5913–5918. [PubMed: 26429265]

Bihan DL, Breton E, Lallemand D, Aubin ML, Vignaud J, Laval-Jeantet M, 1988 Separation of diffusion and perfusion in intravoxel incoherent motion MR imaging. Radiology 168, 497–505. [PubMed: 3393671]

Blackband SJ, Bui JD, Buckley DL, Zelles T, Plant HD, Inglis BA, Phillips MI, 1997 MR microscopy of perfused brain slices. Magnetic Resonance in Medicine 38, 1012–1015. [PubMed: 9402203]

Bloembergen N, Purcell EM, Pound RV, 1948 Relaxation Effects in Nuclear Magnetic Resonance Absorption. Physical Review Online Archive (Prola) 73, 679–712.

Borgia GC, 1996 The effect of diffusion and susceptibility differences on T2 measurements for fluids in porous media and biological tissues. 731–736.

Boss M, Chenevert T, Jackson E, Attariwala R, Shukla-Dave A, Amaro E, Shiroishi M, Wu O, Malyarenko D, Kirsch J, 2015 Multicenter Study of Reproducibility of Wide Range of ADC at 0 °C, Radiological Society of North America 2015 Scientific Assembly and Annual Meeting, Chicago IL.

Boujraf S, Luypaert R, Eisendrath H, Osteaux M, 2001 Echo planar magnetic resonance imaging of anisotropic diffusion in asparagus stems. Magnetic Resonance Materials in Physics, Biology and Medicine 13, 82–90.

Boulby PA, Rugg–Gunn FJ, 2004 T2: The Transverse Relaxation Time. Quantitative MRI of the Brain John Wiley & Sons, Ltd, pp. 143–201.

Bovey FA, Jelinski L, Mirau PA, 1988 CHAPTER 3 - THE CHEMICAL SHIFT Nuclear Magnetic Resonance Spectroscopy (Second Edition). Academic Press, San Diego, pp. 87–146.

Boxerman JL, Hamberg LM, Rosen BR, Weisskoff RM, 1995 MR contrast due to intravascular magnetic susceptibility perturbations. Magn Reson Med 34, 555–566. [PubMed: 8524024]

Budde MD, Frank JA, 2010 Neurite beading is sufficient to decrease the apparent diffusion coefficient after ischemic stroke. Proc Natl Acad Sci U S A 107, 14472–14477. [PubMed: 20660718]

Burcaw LM, Fieremans E, Novikov DS, 2015 Mesoscopic structure of neuronal tracts from timedependent diffusion. NeuroImage 114, 18–37. [PubMed: 25837598]

Callaghan PT, 1993 Principles of nuclear magnetic resonance microscopy. Oxford University Press on Demand.

Callaghan PT, 1995 Pulsed-Gradient Spin-Echo NMR for Planar, Cylindrical, and Spherical Pores under Conditions of Wall Relaxation. Journal of Magnetic Resonance, Series A 113, 53–59.

Callaghan PT, 1997 A simple matrix formalism for spin echo analysis of restricted diffusion under generalized gradient waveforms. J Magn Reson 129, 74–84. [PubMed: 9405218]

Caminiti R, Carducci F, Piervincenzi C, Battaglia-Mayer A, Confalone G, Visco-Comandini F, Pantano P, Innocenti GM, 2013 Diameter, Length, Speed, and Conduction Delay of Callosal Axons in Macaque Monkeys and Humans: Comparing Data from Histology and Magnetic Resonance Imaging Diffusion Tractography. The Journal of Neuroscience 33, 14501. [PubMed: 24005301]

Caminiti R, Ghaziri H, Galuske R, Hof PR, Innocenti GM, 2009 Evolution amplified processing with temporally dispersed slow neuronal connectivity in primates. Proceedings of the National Academy of Sciences 106, 19551–19556.

Capuani S, Palombo M, Gabrielli A, Orlandi A, Maraviglia B, Pastore FS, 2013 Spatio-temporal anomalous diffusion imaging: results in controlled phantoms and in excised human meningiomas. Magn Reson Imaging 31, 359–365. [PubMed: 23102948]

Ceckler TL, Wolff SD, Yip V, Simon SA, Balaban RS, 1992. Dynamic and chemical factors affecting water proton relaxation by macromolecules. Journal of Magnetic Resonance (1969) 98, 637645.

Cercignani M, Alexander DC, 2006 Optimal acquisition schemes for in vivo quantitative magnetization transfer MRI. Magn Reson Med 56, 803–810. [PubMed: 16902982]

Chan KW-Y, Wong W-T, 2007 Small molecular gadolinium(III) complexes as MRI contrast agents for diagnostic imaging. Coordination Chemistry Reviews 251, 2428–2451.

Chen J, Hirasaki GJ, Flaum M, 2006 NMR wettability indices: Effect of OBM on wettability and NMR responses. Reservoir Wettability 52, 161–171.

Chenevert TL, Galbán CJ, Ivancevic MK, Rohrer SE, Londy FJ, Kwee TC, Meyer CR, Johnson TD, Rehemtulla A, Ross BD, 2011 Diffusion coefficient measurement using a temperature controlled fluid for quality control in multi-center studies. Journal of magnetic resonance imaging : JMRI 34, 983–987. [PubMed: 21928310]

Cheng Y, Cory DG, 1999 Multiple Scattering by NMR. Journal of the American Chemical Society 121, 7935–7936.

Chin CL, Wehrli FW, Hwang SN, Takahashi M, Hackney DB, 2002 Biexponential diffusion attenuation in the rat spinal cord: computer simulations based on anatomic images of axonal architecture. Magn Reson Med 47, 455–460. [PubMed: 11870831]

Cho GY, Kim S, Jensen JH, Storey P, Sodickson DK, Sigmund EE, 2012 A versatile flow phantom for intravoxel incoherent motion MRI. Magnetic Resonance in Medicine 67, 1710–1720. [PubMed: 22114007]

Chu Z, Cohen AR, Muthupillai R, Chung T, Wang ZJ, 2004 MRI measurement of hepatic magnetic susceptibility—Phantom validation and normal subject studies. Magnetic Resonance in Medicine 52, 1318–1327. [PubMed: 15562494]

Cook P, Bai Y, Nedjati-Gilani S, Seunarine K, Hall M, Parker G, Alexander D, 2006 Camino: open-source diffusion-MRI reconstruction and processing. Proceedings of the 14th Annual Meeting of ISMRM Seattle WA, USA, p. 2759.

Cory DG, Garroway AN, 1990 Measurement of translational displacement probabilities by NMR: an indicator of compartmentation. Magn Reson Med 14, 435–444. [PubMed: 2355827]

Cronin MJ, 2016 Investigating the effects of microstructure and magnetic susceptibility in MRI., Sir Peter Mansfield Imaging Centre, School of Physics and Astronomy. University of Nottingham, p. 180.

Cronin MJ, Bowtell R, 2018 Quantifying MRI frequency shifts due to structures with anisotropic magnetic susceptibility using pyrolytic graphite sheet. Scientific Reports 8, 6259. [PubMed: 29674616]

De Santis S, Jones DK, Roebroeck A, 2016 Including diffusion time dependence in the extra-axonal space improves in vivo estimates of axonal diameter and density in human white matter. NeuroImage 130, 91–103. [PubMed: 26826514]

Deene YD, Hanselaer P, Wagter CD, Achten E, Neve WD, 2000 An investigation of the chemical stability of a monomer/polymer gel dosimeter. Physics in Medicine & Biology 45, 859. [PubMed: 10795977]

Deistung A, Reichenbach JR, 2011 Effects of Contrast Agents in Susceptibility Weighted Imaging Susceptibility Weighted Imaging in MRI. John Wiley & Sons, Inc., pp. 487–515.

Delakis I, Moore EM, Leach MO, De Wilde JP, 2004 Developing a quality control protocol for diffusion imaging on a clinical MRI system. Phys Med Biol 49, 1409–1422. [PubMed: 15152682]

Does MD, 2018 Inferring brain tissue composition and microstructure via MR relaxometry. NeuroImage.

Does MD, Zhong J, Gore JC, 1999 In vivo measurement of ADC change due to intravascular susceptibility variation. Magnetic Resonance in Medicine 41, 236–240. [PubMed: 10080268]

Donev A, Torquato S, Stillinger FH, 2005 Neighbor list collision-driven molecular dynamics simulation for nonspherical hard particles. I. Algorithmic details. Journal of Computational Physics 202, 737–764.

Dowell NG, Tofts PS, 2010 Quality Assurance for Diffusion MRI In: Jones D (Ed.), Diffusion MRI: Theory, Methods and Applications. Oxford University Press, Oxford.

Dyrby TB, S∅gaard LV, Hall MG, Ptito M, Alexander DC, 2013 Contrast and stability of the axon diameter index from microstructure imaging with diffusion MRI. Magnetic Resonance in Medicine 70, 711–721. [PubMed: 23023798]

Easteal AJ, Price WE, Woolf LA, 1989 Diaphragm cell for high-temperature diffusion measurements. Tracer Diffusion coefficients for water to 363 K. Journal of the Chemical Society, Faraday Transactions 1: Physical Chemistry in Condensed Phases 85, 1091–1097.

Einstein A, 1905 On the motion of small particles suspended in liquids at rest required by the molecular-kinetic theory of heat. Annalen der physik 17, 549–560.

Eriksson S, Lasic S, Topgaard D, 2013 Isotropic diffusion weighting in PGSE NMR by magic-angle spinning of the q-vector. Journal of Magnetic Resonance 226, 13–18. [PubMed: 23178533]

Ernest LM, Maritza AH, Hairong S, Tomy V, Gary RF, 2005 Tissue-mimicking agar/gelatin materials for use in heterogeneous elastography phantoms. Physics in Medicine & Biology 50, 5597. [PubMed: 16306655]

Fan Q, Nummenmaa A, Wichtmann B, Witzel T, Mekkaoui C, Schneider W, Wald LL, Huang SY, 2018 Validation of diffusion MRI estimates of compartment size and volume fraction in a biomimetic brain phantom using a human MRI scanner with 300 mT/m maximum gradient strength. NeuroImage.

Farrher E, Kaffanke J, Celik AA, Stocker T, Grinberg F, Shah NJ, 2012 Novel multisection design of anisotropic diffusion phantoms. Magn Reson Imaging 30, 518–526. [PubMed: 22285876]

Farrher E, Lindemeyer J, Grinberg F, Oros-Peusquens A-M, Shah NJ, 2017 Concerning the matching of magnetic susceptibility differences for the compensation of background gradients in anisotropic diffusion fibre phantoms. PLOS ONE 12, e0176192. [PubMed: 28467458]

Fieremans E, 2008 Validation methods for diffusion weighted magnetic resonance imaging in brain white matter. Department of Electronics and Information Systems. Ghent University, Ghent, Belgium, p. 182.

Fieremans E, De Deene Y, Delputte S, Ozdemir MS, Achten E, Lemahieu I, 2008a The design of anisotropic diffusion phantoms for the validation of diffusion weighted magnetic resonance imaging. Physics in Medicine and Biology 53, 5405–5419. [PubMed: 18765890]

Fieremans E, De Deene Y, Delputte S, Ozdemir MS, D'Asseler Y, Vlassenbroeck J, Deblaere K, Achten E, Lemahieu I, 2008b Simulation and experimental verification of the diffusion in an anisotropic fiber phantom. Journal of Magnetic Resonance 190, 189–199. [PubMed: 18023218]

Fieremans E, Jensen JH, Helpern JA, Kim S, Grossman RI, Inglese M, Novikov DS, 2012a Diffusion distinguishes between axonal loss and demyelination in brain white matter. Proceedings of the 20th Annual Meeting of the International Society for Magnetic Resonance in Medicine.

Fieremans E, Novikov DS, Jensen JH, Helpern JA, 2010 Monte Carlo study of a two-compartment exchange model of diffusion. NMR in Biomedicine 23, 711–724. [PubMed: 20882537]

Fieremans E, Pires A, Jensen JH, 2012b A simple isotropic phantom for diffusional kurtosis imaging. Magnetic Resonance in Medicine 68, 537–542. [PubMed: 22161496]

Fillard P, Descoteaux M, Goh A, Gouttard S, Jeurissen B, Malcolm J, Ramirez-Manzanares A, Reisert M, Sakaie K, Tensaouti F, Yo T, Mangin J-F, Poupon C, 2011 Quantitative evaluation of 10 tractography algorithms on a realistic diffusion MR phantom. NeuroImage 56, 220–234. [PubMed: 21256221]

Ford JC, Hackney DB, 1997 Numerical model for calculation of apparent diffusion coefficients (ADC) in permeable cylinders--comparison with measured ADC in spinal cord white matter. Magn Reson Med 37, 387–394. [PubMed: 9055229]

Fralix TA, Ceckler TL, Wolff SD, Simon SA, Balaban RS, 1991 Lipid bilayer and water proton magnetization transfer: Effect of cholesterol. Magnetic Resonance in Medicine 18, 214–223. [PubMed: 2062233]

Fukuzaki M, Miura N, Shinyashiki N, Kurita D, Shioya S, Haida M, Mashimo S, 1995 Comparison of Water Relaxation Time in Serum Albumin Solution Using Nuclear Magnetic Resonance and Time Domain Reflectometry. The Journal of Physical Chemistry 99, 431–435.

Gaass T, Schneider MJ, Dietrich O, Ingrisch M, Dinkel J, 2017 Technical Note: Quantitative dynamic contrast-enhanced MRI of a 3-dimensional artificial capillary network. Medical Physics 44, 1462–1469. [PubMed: 28235128]

Gagnon L, Sakadzic S, Lesage F, Musacchia JJ, Lefebvre J, Fang Q, Yucel MA, Evans KC, Mandeville ET, Cohen-Adad J, Polimeni JR, Yaseen MA, Lo EH, Greve DN, Buxton RB, Dale AM, Devor A, Boas DA, 2015 Quantifying the microvascular origin of BOLD-fMRI from first principles with two-photon microscopy and an oxygen-sensitive nanoprobe. J Neurosci 35, 3663–3675. [PubMed: 25716864]

Ginsburger K, Poupon F, Beaujoin J, Estournet D, Matuschke F, Mangin JF, Axer M, Poupon C, 2018 Improving the Realism of White Matter Numerical Phantoms: A Step toward a Better Understanding of the Influence of Structural Disorders in Diffusion MRI. Frontiers in Physics 6.

Glantz LA, Lewis DA, 2000 Decreased dendritic spine density on prefrontal cortical pyramidal neurons in schizophrenia. Arch Gen Psychiatry 57, 65–73. [PubMed: 10632234]

Goggin PM, Zygalakis KC, Oreffo RO, Schneider P, 2016 High-resolution 3D imaging of osteocytes and computational modelling in mechanobiology: insights on bone development, ageing, health and disease. Eur Cell Mater 31, 264–295. [PubMed: 27209400]

Gowland PA, Stevenson VL, 2004 T1: The Longitudinal Relaxation Time Quantitative MRI of the Brain. John Wiley & Sons, Ltd, pp. 111–141.

Grebenkov DS, 2010 Pulsed-gradient spin-echo monitoring of restricted diffusion in multilayered structures. J Magn Reson 205, 181–195. [PubMed: 20570195]

Grebenkov DS, 2011 A fast random walk algorithm for computing the pulsed-gradient spin-echo signal in multiscale porous media. J Magn Reson 208, 243–255. [PubMed: 21159532]

Grebenkov DS, 2014 Exploring diffusion across permeable barriers at high gradients. II. Localization regime. J Magn Reson 248, 164–176. [PubMed: 25266755]

Grech-Sollars M, Hales PW, Miyazaki K, Raschke F, Rodriguez D, Wilson M, Gill SK, Banks T, Saunders DE, Clayden JD, Gwilliam MN, Barrick TR, Morgan PS, Davies NP, Rossiter J, Auer DP, Grundy R, Leach MO, Howe FA, Peet AC, Clark CA, 2015 Multi-centre reproducibility of diffusion MRI parameters for clinical sequences in the brain. NMR in Biomedicine 28, 468–485. [PubMed: 25802212]

Grossman RI, 1999 Application of magnetization transfer imaging to multiple sclerosis. Neurology 53, S8–11. [PubMed: 10496204]

Guise C, Fernandes MM, Nóbrega JM, Pathak S, Schneider W, Fangueiro R, 2016 Hollow Polypropylene Yarns as a Biomimetic Brain Phantom for the Validation of High-Definition Fiber Tractography Imaging. ACS Applied Materials & Interfaces 8, 29960–29967. [PubMed: 27723307]

Hagslatt H, Jonsson B, Nyden M, Soderman O, 2003 Predictions of pulsed field gradient NMR echo-decays for molecules diffusing in various restrictive geometries. Simulations of diffusion propagators based on a finite element method. J Magn Reson 161, 138–147. [PubMed: 12713963]

Hall M, Nedjati-Gilani G, Alexander D, 2014 Monte-Carlo simulation of diffusion MRI with realistic voxel sizes. Proceedings of the 22nd Annual Meeting of ISMRM.

Hall MG, Alexander DC, 2009 Convergence and parameter choice for Monte-Carlo simulations of diffusion MRI. IEEE Trans Med Imaging 28, 1354–1364. [PubMed: 19273001]

Hara M, Kuroda M, Ohmura Y, Matsuzaki H, Kobayashi T, Murakami J, Katashima K, Ashida M, Ohno S, Asaumi JI, 2014 A new phantom and empirical formula for apparent diffusion coefficient measurement by a 3 Tesla magnetic resonance imaging scanner. Oncol Lett 8, 819–824. [PubMed: 25013504]

Harkins KD, Does MD, 2016 Simulations on the influence of myelin water in diffusion-weighted imaging. Phys Med Biol 61, 4729–4745. [PubMed: 27271991]

Harkins KD, Galons JP, Secomb TW, Trouard TP, 2009 Assessment of the effects of cellular tissue properties on ADC measurements by numerical simulation of water diffusion. Magn Reson Med 62, 1414–1422. [PubMed: 19785014]

Hellerbach A, Schuster V, Jansen A, Sommer J, 2013 MRI Phantoms – Are There Alternatives to Agar? PLOS ONE 8, e70343. [PubMed: 23940563]

Hellwig B, Schuz A, Aertsen A, 1994 Synapses on axon collaterals of pyramidal cells are spaced at random intervals: a Golgi study in the mouse cerebral cortex. Biol Cybern 71, 1–12. [PubMed: 7519886]

Henkelman RM, Huang X, Xiang Q-S, Stanisz GJ, Swanson SD, Bronskill MJ, 1993 Quantitative interpretation of magnetization transfer. Magnetic Resonance in Medicine 29, 759–766. [PubMed: 8350718]

Hills B, 1998 Magnetic Resonance Imaging in Food Science. Wiley.

Holz M, Heil SR, Sacco A, 2000 Temperature-dependent self-diffusion coefficients of water and six selected molecular liquids for calibration in accurate 1H NMR PFG measurements. Physical Chemistry Chemical Physics 2, 4740–4742.

Hubbard PL, Zhou F-L, Eichhorn SJ, Parker GJM, 2015 Biomimetic phantom for the validation of diffusion magnetic resonance imaging. Magnetic Resonance in Medicine 73, 299–305. [PubMed: 24469863]

Hwang SN, Chin CL, Wehrli FW, Hackney DB, 2003 An image-based finite difference model for simulating restricted diffusion. Magn Reson Med 50, 373–382. [PubMed: 12876714]

Innocenti GM, Caminiti R, Aboitiz F, 2015. Comments on the paper by Horowitz et al. (2014). Brain Structure and Function 220, 1789–1790.

Jelescu IO, Budde MD, 2017 Design and Validation of Diffusion MRI Models of White Matter. Frontiers in Physics 5

Jensen JH, Chandra R, 2000a NMR relaxation in tissues with weak magnetic inhomogeneities. Magnetic Resonance in Medicine 44, 144–156. [PubMed: 10893533]

Jensen JH, Chandra R, 2000b Strong field behavior of the NMR signal from magnetically heterogeneous tissues. Magnetic Resonance in Medicine 43, 226–236. [PubMed: 10680686]

Jensen JH, Chandra R, Ramani A, Lu H, Johnson G, Lee SP, Kaczynski K, Helpern JA, 2006 Magnetic field correlation imaging. Magnetic Resonance in Medicine 55, 1350–1361. [PubMed: 16700026]

Jensen JH, Helpern JA, 2010 MRI quantification of non-Gaussian water diffusion by kurtosis analysis. NMR Biomed 23, 698–710. [PubMed: 20632416]

Jensen JH, Helpern JA, Ramani A, Lu H, Kaczynski K, 2005 Diffusional kurtosis imaging: the quantification of non-gaussian water diffusion by means of magnetic resonance imaging. Magn Reson Med 53, 1432–1440. [PubMed: 15906300]

Jones C, MacKay A, Rutt B, 1998 Bi-Exponential T2 Decay in Dairy Cream Phantoms. Magn Reson Imaging 16, 83–85. [PubMed: 9436951]

Karampinos DC, King KF, Sutton BP, Georgiadis JG, 2010 Intravoxel partially coherent motion technique: Characterization of the anisotropy of skeletal muscle microvasculature. Journal of Magnetic Resonance Imaging 31, 942–953. [PubMed: 20373440]

Keenan KE, Ainslie M, Barker AJ, Boss MA, Cecil KM, Charles C, Chenevert TL, Clarke L, Evelhoch JL, Finn P, Gembris D, Gunter JL, Hill DLG, Jack CR, Jr., Jackson EF, Liu G, Russek SE, Sharma SD, Steckner M, Stupic KF, Trzasko JD, Yuan C, Zheng J, 2018 Quantitative magnetic resonance imaging phantoms: A review and the need for a system phantom. Magn Reson Med 79, 48–61. [PubMed: 29083101]

Kennan RP, Gao JH, Zhong J, Gore JC, 1994 A general model of microcirculatory blood flow effects in gradient sensitized MRI. Med Phys 21, 539–545. [PubMed: 8058020]

Kiselev VG, 2004 Effect of magnetic field gradients induced by microvasculature on NMR measurements of molecular self-diffusion in biological tissues. Journal of Magnetic Resonance 170, 228235.

Kiselev VG, 2010 The cumulant expansion: an overarching mathematical framework for understanding diffusion NMR In: Jones DK (Ed.), Diffusion MRI. Oxford University Press, p. 152.

Kiselev VG, Posse S, 1999 Analytical model of susceptibility-induced MR signal dephasing: Effect of diffusion in a microvascular network. Magnetic Resonance in Medicine 41, 499–509. [PubMed: 10204873]

Kleinberg RL, 1996 Utility of NMR T2 distributions, connection with capillary pressure, clay effect, and determination of the surface relaxivity parameter rho2. 761–767.

Kłodowski K, Krzyżak AT, 2016 Innovative anisotropic phantoms for calibration of diffusion tensor imaging sequences. Magn Reson Imaging 34, 404–409. [PubMed: 26707852]

Koch MA, Finsterbusch J, 2008 Compartment size estimation with double wave vector diffusionweighted imaging. Magnetic Resonance in Medicine 60, 90–101. [PubMed: 18421690]

Koenig SH, Brown RD, 3rd, Ugolini R, 1993 Magnetization transfer in cross-linked bovine serum albumin solutions at 200 MHz: a model for tissue. Magn Reson Med 29, 311–316. [PubMed: 8383788]

Komlosh ME, Benjamini D, Barnett AS, Schram V, Horkay F, Avram AV, Basser PJ, 2017 Anisotropic phantom to calibrate high-q diffusion MRI methods. Journal of Magnetic Resonance 275, 19–28. [PubMed: 27951427]

Komlosh ME, Horkay F, Freidlin RZ, Nevo U, Assaf Y, Basser PJ, 2007 Detection of microscopic anisotropy in gray matter and in a novel tissue phantom using double Pulsed Gradient Spin Echo MR. Journal of Magnetic Resonance 189, 38–45. [PubMed: 17869147]

Komlosh ME, Özarslan E, Lizak MJ, Horkay F, Schram V, Shemesh N, Cohen Y, Basser PJ, 2011 Pore diameter mapping using double pulsed-field gradient MRI and its validation using a novel glass capillary array phantom. Journal of Magnetic Resonance 208, 128–135. [PubMed: 21084204]

Krzyżak AT, Olejniczak Z, 2015 Improving the accuracy of PGSE DTI experiments using the spatial distribution of b matrix. Magn Reson Imaging 33, 286–295. [PubMed: 25460327]

Kucharczyk W, Macdonald PM, Stanisz GJ, Henkelman RM, 1994 Relaxivity and magnetization transfer of white matter lipids at MR imaging: importance of cerebrosides and pH. Radiology 192, 521529.

Lam WW, Jbabdi S, Miller KL, 2015 A model for extra-axonal diffusion spectra with frequencydependent restriction. Magn Reson Med 73, 2306–2320. [PubMed: 25046481]

Landman BA, Farrell JA, Smith SA, Reich DS, Calabresi PA, van Zijl PC, 2010 Complex geometric models of diffusion and relaxation in healthy and damaged white matter. NMR Biomed 23, 152–162. [PubMed: 19739233]

Lasič S, Nilsson M, Lätt J, Ståhlberg F, Topgaard D, 2011 Apparent exchange rate mapping with diffusion MRI. Magnetic Resonance in Medicine 66, 356–365. [PubMed: 21446037]

Lasič S, Szczepankiewicz F, Eriksson S, Nilsson M, Topgaard D, 2014 Microanisotropy imaging: quantification of microscopic diffusion anisotropy and orientational order parameter by diffusion MRI with magic-angle spinning of the q-vector. Frontiers in Physics 2.

Latour LL, Svoboda K, Mitra PP, Sotak CH, 1994 Time-dependent diffusion of water in a biological model system. Proc Natl Acad Sci U S A 91, 1229–1233. [PubMed: 8108392]

Lätt J, Nilsson M, Rydhög A, Wirestam R, Ståhlberg F, Brockstedt S, 2007 Effects of restricted diffusion in a biological phantom: a q-space diffusion MRI study of asparagus stems at a 3T clinical scanner. Magnetic Resonance Materials in Physics, Biology and Medicine 20, 213–222.

Laubach HJ, Jakob PM, Loevblad KO, Baird AE, Bovo MP, Edelman RR, Warach S, 1998 A phantom for diffusion-weighted imaging of acute stroke. J Magn Reson Imaging 8, 1349–1354. [PubMed: 9848751]

Laun FB, Huff S, Stieltjes B, 2009 On the effects of dephasing due to local gradients in diffusion tensor imaging experiments: relevance for diffusion tensor imaging fiber phantoms. Magn Reson Imaging 27, 541–548. [PubMed: 18977104]

Lavdas I, Behan KC, Papadaki A, McRobbie DW, Aboagye EO, 2013 A phantom for diffusionweighted MRI (DW-MRI). Journal of Magnetic Resonance Imaging 38, 173–179. [PubMed: 23576443]

Lebois A, Yeh C-H, Le Bihan D, Mangin J-F, Lin C, Poupon C, 2013a Axon diameter mapping: Gaussian phase distribution approximation of the diffusion signal attenuation using a two-pool thick layer cylinder model Diffusion as a Probe of Neural Tissue Microstructure, Podstrana, Croatia.

Lebois A, Yeh C-H, Le Bihan D, Mangin J-F, Lin C, Poupon C, 2013b Cell diameter mapping: Gaussian phase distribution approximation of the diffusion signal attenuation using a two-pool thick layer sphere model Diffusion as a Probe of Neural Tissue Microstructure, Podstrana, Croatia.

Lee H-H, Fieremans E, Novikov DS, 2017a What dominates the time dependence of diffusion transverse to axons: Intra-or extra-axonal water? NeuroImage.

Lee J-S, Regatte RR, Jerschow A, 2017b Magnetization transfer in a partly deuterated lyotropic liquid crystal by single- and dual-frequency RF irradiations. Journal of Magnetic Resonance 281, 141150.

Lee JH, Cheong H, Lee SS, Lee CK, Sung YS, Huh J-W, Song J-A, Choe H, 2016 Perfusion Assessment Using Intravoxel Incoherent Motion-Based Analysis of Diffusion-Weighted

Magnetic Resonance Imaging: Validation Through Phantom Experiments. Investigative Radiology 51, 520–528. [PubMed: 26895196]

Lemberskiy G, Baete SH, Cloos MA, Novikov DS, Fieremans E, 2017 Validation of surface-to-volume ratio measurements derived from oscillating gradient spin echo on a clinical scanner using anisotropic fiber phantoms. NMR in Biomedicine 30, n/a-n/a.

Li H, Gore JC, Xu J, 2014a Fast and robust measurement of microstructural dimensions using temporal diffusion spectroscopy. Journal of Magnetic Resonance 242, 4–9. [PubMed: 24583517]

Li JR, Nguyen HT, Nguyen DV, Haddar H, Coatleven J, Le Bihan D, 2014b Numerical study of a macroscopic finite pulse model of the diffusion MRI signal. J Magn Reson 248, 54–65. [PubMed: 25314082]

Li K, Zu Z, Xu J, Janve VA, Gore JC, Does MD, Gochberg DF, 2010 Optimized inversion recovery sequences for quantitative T1 and magnetization transfer imaging. Magn Reson Med 64, 491500.

Li W, Wu B, Liu C, 2011 Quantitative susceptibility mapping of human brain reflects spatial variation in tissue composition. NeuroImage 55, 1645–1656. [PubMed: 21224002]

Liang Y, Chen W, Akpa BS, Neuberger T, Webb AG, Magin RL, 2017 Using spectral and cumulative spectral entropy to classify anomalous diffusion in Sephadex™ gels. Computers & Mathematics with Applications 73, 765–774.

Liewald D, Miller R, Logothetis N, Wagner HJ, Schuz A, 2014 Distribution of axon diameters in cortical white matter: an electron-microscopic study on three human brains and a macaque. Biol Cybern 108, 541–557. [PubMed: 25142940]

Lin C-P, Wedeen V, Chen J-H, Yao C, Tseng W-Y, 2003 Validation of diffusion spectrum magnetic resonance imaging with manganese-enhanced rat optic tracts and ex vivo phantoms. NeuroImage 19, 482–495. [PubMed: 12880782]

Lin M, He H, Schifitto G, Zhong J, 2016 Simulation of changes in diffusion related to different pathologies at cellular level after traumatic brain injury. Magn Reson Med 76, 290–300. [PubMed: 26256558]

Lin M, He H, Tong Q, Ding Q, Yan X, Feiweier T, Zhong J, 2018 Effect of myelin water exchange on DTI-derived parameters in diffusion MRI: Elucidation of TE dependence. Magn Reson Med 79, 1650–1660. [PubMed: 28656631]

Liu C, Bammer R, Acar B, Moseley ME, 2004 Characterizing non-Gaussian diffusion by using generalized diffusion tensors. Magn Reson Med 51, 924–937. [PubMed: 15122674]

Lorenz CH, Pickens DR, Puffer DB, Price RR, 1991 Magnetic resonance diffusion/perfusion phantom experiments. Magnetic Resonance in Medicine 19, 254–260. [PubMed: 1881312]

Lorenz R, Bellemann EM, Hennig J, Il'yasov AK, 2008 Anisotropic Phantoms for Quantitative Diffusion Tensor Imaging and Fiber-Tracking Validation. Applied Magnetic Resonance 33, 419–429.

Magin RL, Akpa BS, Neuberger T, Webb AG, 2011 Fractional order analysis of Sephadex gel structures: NMR measurements reflecting anomalous diffusion. Communications in Nonlinear Science and Numerical Simulation 16, 4581–4587. [PubMed: 21804746]

Maier SE, Mitsouras D, Mulkern RV, 2014 Avian egg latebra as brain tissue water diffusion model. Magnetic Resonance in Medicine 72, 501–509. [PubMed: 24105853]

Maki JH, Macfall JR, Johnson GA, 1991 The use of gradient flow compensation to separate diffusion and microcirculatory flow in MRI. Magnetic Resonance in Medicine 17, 95–107. [PubMed: 1712421]

Malyarenko DI, Newitt D, Wilmes J, L., Tudorica A., Helmer KG, Arlinghaus LR, Jacobs MA, Jajamovich G, Taouli B, Yankeelov TE, Huang W, Chenevert, TL, 2016 Demonstration of nonlinearity bias in the measurement of the apparent diffusion coefficient in multicenter trials. Magnetic Resonance in Medicine 75, 1312–1323. [PubMed: 25940607]

Malyarenko DI, Zimmermann EM, Adler J, Swanson SD, 2014 Magnetization transfer in lamellar liquid crystals. Magnetic Resonance in Medicine 72, 1427–1434. [PubMed: 24258798]

Mendelson DA, Heinsbergen JF, Kennedy SD, Szczepaniak LS, Lester CC, Bryant RG, 1991 Comparison of agarose and cross-linked protein gels as magnetic resonance imaging phantoms. Magn Reson Imaging 9, 975–978. [PubMed: 1766326]

Merboldt K-D, Hanicke W, Frahm J, 1985. Self-diffusion NMR imaging using stimulated echoes. Journal of Magnetic Resonance (1969) 64, 479–486.

Milne ML, Conradi MS, 2009 Multi-exponential signal decay from diffusion in a single compartment. Journal of Magnetic Resonance 197, 87–90. [PubMed: 19121965]

Mingasson T, Duval T, Stikov N, Cohen-Adad J, 2017 AxonPacking: An Open-Source Software to Simulate Arrangements of Axons in White Matter. Front Neuroinform 11, 5. [PubMed: 28197091]

Mitra PP, Sen PN, Schwartz LM, 1993 Short-time behavior of the diffusion coefficient as a geometrical probe of porous media. PHYSICAL REVIEW. B. CONDENSED MATTER. 47, 8565–8574.

Moroney BF, Stait-Gardner T, Ghadirian B, Yadav NN, Price WS, 2013 Numerical analysis of NMR diffusion measurements in the short gradient pulse limit. J Magn Reson 234, 165–175. [PubMed: 23887027]

Morozov D, Bar L, Sochen N, Cohen Y, 2013 Measuring small compartments with relatively weak gradients by angular double-pulsed-field-gradient NMR. Magn Reson Imaging 31, 401–407. [PubMed: 23102951]

Morozov D, Bar L, Sochen N, Cohen Y, 2015 Microstructural information from angular doublepulsed-field-gradient NMR: From model systems to nerves. Magnetic Resonance in Medicine 74, 25–32. [PubMed: 25042986]

Mougin OE, Coxon RC, Pitiot A, Gowland PA, 2010 Magnetization transfer phenomenon in the human brain at 7 T. NeuroImage 49, 272–281. [PubMed: 19683581]

Mulkern RV, Ricci KI, Vajapeyam S, Chenevert TL, Malyarenko DI, Kocak M, Poussaint TY, 2015 Pediatric Brain Tumor Consortium Multisite Assessment of Apparent Diffusion Coefficient z-Axis Variation Assessed with an Ice–Water Phantom. Academic Radiology 22, 363–369. [PubMed: 25435183]

Neeman M, Freyer JP, Sillerud LO, 1991 A simple method for obtaining cross-term-free images for diffusion anisotropy studies in NMR microimaging. Magnetic Resonance in Medicine 21, 138–143. [PubMed: 1943671]

Nguyen DV, Li J-R, Grebenkov D, Le Bihan D, 2014 A finite elements method to solve the Bloch–Torrey equation applied to diffusion magnetic resonance imaging. Journal of Computational Physics 263, 283–302.

Nilsson M, Alerstam E, Wirestam R, Stahlberg F, Brockstedt S, Latt J, 2010 Evaluating the accuracy and precision of a two-compartment Karger model using Monte Carlo simulations. J Magn Reson 206, 59–67. [PubMed: 20594881]

Nilsson M, Larsson J, Lundberg D, Szczepankiewicz F, Witzel T, Westin C-F, Bryskhe K, Topgaard D, 2018 Liquid crystal phantom for validation of microscopic diffusion anisotropy measurements on clinical MRI systems. Magnetic Resonance in Medicine 79, 1817–1828. [PubMed: 28686785]

Nilsson M, Latt J, Nordh E, Wirestam R, Stahlberg F, Brockstedt S, 2009 On the effects of a varied diffusion time in vivo: is the diffusion in white matter restricted? Magn Reson Imaging 27, 176187.

Nilsson M, Latt J, Stahlberg F, van Westen D, Hagslatt H, 2012 The importance of axonal undulation in diffusion MR measurements: a Monte Carlo simulation study. NMR Biomed 25, 795–805. [PubMed: 22020832]

Novikov D, Jensen J, Helpern J, 2009 Permeability and surface area of cell membranes from the DWI signal. Proceedings of the 17th Annual Meeting of ISMRM, p. 451.

Novikov D, Jespersen S, Kiselev V, Fieremans E, 2016 Quantifying brain microstructure with diffusion MRI: Theory and parameter estimation.

Novikov D, Kiselev V, 2008 Transverse NMR relaxation in magnetically heterogeneous media. Journal of Magnetic Resonance 195, 33–39. [PubMed: 18824379]

Novikov DS, Fieremans E, Jensen JH, Helpern JA, 2011 Random walks with barriers. Nature Physics 7, 508. [PubMed: 21686083]

Novikov DS, Jensen JH, Helpern JA, Fieremans E, 2014 Revealing mesoscopic structural universality with diffusion. Proc Natl Acad Sci U S A 111, 5088–5093. [PubMed: 24706873]

Novikov DS, Kiselev VG, 2010 Effective medium theory of a diffusion-weighted signal. NMR Biomed 23, 682–697. [PubMed: 20886563]

Novikov DS, Kiselev VG, 2011 Surface-to-volume ratio with oscillating gradients. J Magn Reson 210, 141–145. [PubMed: 21393035]

Novikov DS, Kiselev VG, Jespersen SN, 2018 On modeling. Magnetic Resonance in Medicine 79, 3172–3193. [PubMed: 29493816]

Novikov DS, Reisert M, Kiselev VG, 2012 Susceptibility-induced increase of apparent diffusion coefficient: BOLD effect behind diffusion fMRI. 20th Annual Meeting of the International Society for Magnetic Resonance in Medicine, 2072.

Ohno N, Miyati T, Chigusa T, Usui H, Ishida S, Hiramatsu Y, Kobayashi S, Gabata T, Alperin N, 2017 Technical Note: Development of a cranial phantom for assessing perfusion, diffusion, and biomechanics. Medical Physics 44, 1646–1654. [PubMed: 28241107]

Oros-Peusquens AM, Laurila M, Shah NJ, 2008 Magnetic field dependence of the distribution of NMR relaxation times in the living human brain. Magnetic Resonance Materials in Physics, Biology and Medicine 21, 131.

Palacios EM, Martin AJ, Boss MA, Ezekiel F, Chang YS, Yuh EL, Vassar MJ, Schnyer DM, MacDonald CL, Crawford KL, Irimia A, Toga AW, Mukherjee P, 2017 Toward Precision and Reproducibility of Diffusion Tensor Imaging: A Multicenter Diffusion Phantom and Traveling Volunteer Study. American Journal of Neuroradiology 38, 537–545. [PubMed: 28007768]

Palombo M, Ligneul C, Hernandez-Garzon E, Valette J, 2017 Can we detect the effect of spines and leaflets on the diffusion of brain intracellular metabolites? NeuroImage.

Pampel A, Jochimsen Thies H, Möller Harald E, 2010 BOLD background gradient contributions in diffusion-weighted fMRI—comparison of spin-echo and twice-refocused spin-echo sequences. NMR in Biomedicine 23, 610–618. [PubMed: 20235336]

Pan D, Caruthers SD, Senpan A, Schmieder AH, Wickline SA, Lanza GM, 2011 Revisiting an old friend: manganese-based MRI contrast agents. Wiley Interdiscip Rev Nanomed Nanobiotechnol 3, 162–173. [PubMed: 20860051]

Panagiotaki E, Hall MG, Zhang H, Siow B, Lythgoe MF, Alexander DC, 2010 High-fidelity meshes from tissue samples for diffusion MRI simulations. Med Image Comput Comput Assist Interv 13, 404–411. [PubMed: 20879341]

Papaioannou A, Novikov DS, Fieremans E, Boutis GS, 2017 Observation of structural universality in disordered systems using bulk diffusion measurement. Physical Review E 96, 061101. [PubMed: 29347412]

Peled S, 2007 New perspectives on the sources of white matter DTI signal. IEEE Trans Med Imaging 26, 1448–1455. [PubMed: 18041260]

Pierpaoli C, Basser PJ, 1996 Toward a quantitative assessment of diffusion anisotropy. Magn Reson Med 36, 893–906. [PubMed: 8946355]

Pierpaoli C, Sarlls J, Nevo U, Basser PJ, Horkay F, 2008 Polyvinylpyrrolidone (PVP) water solutions as isotropic phantoms for diffusion MRI studies. 16th Annual Meeting of the International Society for Magnetic Resonance in Medicine, Toronto, p. 1414.

Poupon C, Rieul B, Kezele I, Perrin M, Poupon F, Mangin JF, 2008 New diffusion phantoms dedicated to the study and validation of high-angular-resolution diffusion imaging (HARDI) models. Magn Reson Med 60, 1276–1283. [PubMed: 19030160]

Powles JG, Mallett M, Rickayzen G, Evans W, 1992 Exact analytic solutions for diffusion impeded by an infinite array of partially permeable barriers Proceedings of the Royal Society of London A: Mathematical, Physical and Engineering Sciences. The Royal Society, pp. 391–403.

Price WS, 2009 NMR Studies of Translational Motion: Principles and Applications. Cambridge University Press, Cambridge.

Pullens P, Roebroeck A, Goebel R, 2010 Ground truth hardware phantoms for validation of diffusion-weighted MRI applications. J Magn Reson Imaging 32, 482–488. [PubMed: 20677281]

Ramirez-Manzanares A, Cook PA, Hall M, Ashtari M, Gee JC, 2011 Resolving axon fiber crossings at clinical b-values: an evaluation study. Med Phys 38, 5239–5253. [PubMed: 21978068]

Reischauer C, Staempfli P, Jaermann T, Boesiger P, 2009 Construction of a temperature-controlled diffusion phantom for quality control of diffusion measurements. Journal of Magnetic Resonance Imaging 29, 692–698. [PubMed: 19243053]

Richardson S, Siow B, Batchelor AM, Lythgoe MF, Alexander DC, 2013 A viable isolated tissue system: A tool for detailed MR measurements and controlled perturbation in physiologically stable tissue. Magnetic Resonance in Medicine 69, 1603–1610. [PubMed: 22821404]

Ruh A, Scherer H, Kiselev VG, 2018 The larmor frequency shift in magnetically heterogeneous media depends on their mesoscopic structure. Magn Reson Med 79, 1101–1110. [PubMed: 28524556]

Russell G, Harkins KD, Secomb TW, Galons JP, Trouard TP, 2012 A finite difference method with periodic boundary conditions for simulations of diffusion-weighted magnetic resonance experiments in tissue. Phys Med Biol 57, N35–46. [PubMed: 22297418]

Salomir R, de Senneville BD, Moonen CTW, 2003 A fast calculation method for magnetic field inhomogeneity due to an arbitrary distribution of bulk susceptibility. Concepts in Magnetic Resonance Part B: Magnetic Resonance Engineering 19B, 26–34.

Schachter M, Does MD, Anderson AW, Gore JC, 2000 Measurements of restricted diffusion using an oscillating gradient spin-echo sequence. J Magn Reson 147, 232–237. [PubMed: 11097814]

Schindelin J, Arganda-Carreras I, Frise E, Kaynig V, Longair M, Pietzsch T, Preibisch S, Rueden C, Saalfeld S, Schmid B, Tinevez JY, White DJ, Hartenstein V, Eliceiri K, Tomancak P, Cardona A, 2012 Fiji: an open-source platform for biological-image analysis. Nat Methods 9, 676682.

Schmierer K, Wheeler-Kingshott CAM, Boulby PA, Scaravilli F, Altmann DR, Barker GJ, Tofts PS, Miller DH, 2007 Diffusion tensor imaging of post mortem multiple sclerosis brain. NeuroImage 35, 467–477. [PubMed: 17258908]

Schneider MGTD, Julien; Ingrisch, Michael; Reiser, Maximilian F; Dietrich Olaf, 2016 Intravoxel Incoherent Motion MRI in a 3-Dimensional Microvascular Flow Phantom. Annual Meeting of the International Society for Magnetic Resonance in Medicine, Signapore, p. 0920.

Schrader MEL, George I (Ed.), 1992 Modern Approaches to Wettability.

Selwyn R, 2014 Phantoms for Magnetic Resonance Imaging In: DeWerd LA, Kissick M (Eds.), The Phantoms of Medical and Health Physics: Devices for Research and Development. Springer New York, New York, NY, pp. 181–199.

Sen PN, Basser PJ, 2005 A model for diffusion in white matter in the brain. Biophys J 89, 2927–2938. [PubMed: 16100258]

Sen PN, Schwartz LM, Mitra PP, Halperin BI, 1994 Surface relaxation and the long-time diffusion coefficient in porous media: Periodic geometries. PHYSICAL REVIEW. B. CONDENSED MATTER. 49, 215–225.

Shemesh N, Adiri T, Cohen Y, 2011 Probing Microscopic Architecture of Opaque Heterogeneous Systems Using Double-Pulsed-Field-Gradient NMR. Journal of the American Chemical Society 133, 6028–6035. [PubMed: 21446740]

Shemesh N, Ozarslan E, Basser PJ, Cohen Y, 2010 Detecting diffusion-diffraction patterns in size distribution phantoms using double-pulsed field gradient NMR: Theory and experiments. Journal of Chemical Physics 132, 034703. [PubMed: 20095748]

Shemesh N, Özarslan E, Basser PJ, Cohen Y, 2012 Accurate noninvasive measurement of cell size and compartment shape anisotropy in yeast cells using double-pulsed field gradient MR. NMR in Biomedicine 25, 236–246. [PubMed: 21786354]

Shepherd GM, Raastad M, Andersen P, 2002 General and variable features of varicosity spacing along unmyelinated axons in the hippocampus and cerebellum. Proc Natl Acad Sci U S A 99, 6340–6345. [PubMed: 11972022]

Shepherd TM, Flint J, Thelwall PE, Stanisz GJ, Mareci TH, Yachnis AT, Blackband SJ, 2009a Postmortem interval alters the water relaxation and diffusion properties of rat nervous tissue – Implications for MRI studies of human autopsy samples. NeuroImage 44, 820–826. [PubMed: 18996206]

Shepherd TM, Thelwall PE, Stanisz GJ, Blackband SJ, 2009b Aldehyde fixative solutions alter the water relaxation and diffusion properties of nervous tissue. Magnetic Resonance in Medicine 62, 26–34. [PubMed: 19353660]

Shmueli K, de Zwart JA, van Gelderen P, Li T-Q, Dodd SJ, Duyn JH, 2009 Magnetic susceptibility mapping of brain tissue in vivo using MRI phase data. Magnetic Resonance in Medicine 62, 1510–1522. [PubMed: 19859937]

Sigmund EE, Song Y-Q, 2006 Multiple echo diffusion tensor acquisition technique. Magn Reson Imaging 24, 7–18. [PubMed: 16410173]

Silva MD, Helmer KG, Lee J-H, Han SS, Springer CS, Sotak CH, 2002 Deconvolution of Compartmental Water Diffusion Coefficients in Yeast-Cell Suspensions Using Combined T1 and Diffusion Measurements. Journal of Magnetic Resonance 156, 52–63. [PubMed: 12081442]

Siow B, Drobnjak I, Chatterjee A, Lythgoe MF, Alexander DC, 2012 Estimation of pore size in a microstructure phantom using the optimised gradient waveform diffusion weighted NMR sequence. Journal of Magnetic Resonance 214, 51–60. [PubMed: 22116034]

Skoge M, Donev A, Stillinger FH, Torquato S, 2006 Packing hyperspheres in high-dimensional Euclidean spaces. Physical Review E 74, 041127.

Slijkerman WF, Hofman JP, 1998 Determination of surface relaxivity from NMR diffusion measurements. Magn Reson Imaging 16, 541–544. [PubMed: 9803905]

Spees WM, Song SK, Garbow JR, Neil JJ, Ackerman JJ, 2012 Use of ethylene glycol to evaluate gradient performance in gradient-intensive diffusion MR sequences. Magn Reson Med 68, 319–324. [PubMed: 22127787]

Stanisz GJ, 2003 Diffusion MR in Biological Systems: Tissue Compartments and Exchange. Israel Journal of Chemistry 43, 33–44.

Stanisz GJ, Li JG, Wright GA, Henkelman RM, 1998 Water dynamics in human blood via combined measurements of T2 relaxation and diffusion in the presence of gadolinium. Magn Reson Med 39, 223–233. [PubMed: 9469705]

Stanisz GJ, Szafer A, Wright GA, Henkelman RM, 1997 An analytical model of restricted diffusion in bovine optic nerve. Magn Reson Med 37, 103–111. [PubMed: 8978638]

Stejskal EO, 1965 Use of Spin Echoes in a Pulsed Magnetic-Field Gradient to Study Anisotropic, Restricted Diffusion and Flow. The Journal of Chemical Physics 43, 3597–3603.

Stikov N, Perry LM, Mezer A, Rykhlevskaia E, Wandell BA, Pauly JM, Dougherty RF, 2011 Bound pool fractions complement diffusion measures to describe white matter micro and macrostructure. NeuroImage 54, 1112–1121. [PubMed: 20828622]

Stoll ME, Majors TJ, 1982 Reduction of magnetic susceptibility broadening in NMR by susceptibility matching. Journal of Magnetic Resonance (1969) 46, 283–288.

Swanson S, Malyarenko D, Schmiedlin-Ren P, Adler J, Helvie K, Reingold L, Al-Hawary M, Zimmerman E, 2012 Lamellar liquid crystal phantoms for MT-calibration and quality control in clinical studies. Proceedings of the 20th Annual Meeting of the ISMRM, Melbourne, p. 1378.

Szafer A, Zhong J, Gore JC, 1995 Theoretical model for water diffusion in tissues. Magn Reson Med 33, 697–712. [PubMed: 7596275]

Tanner JE, 1970 Use of the Stimulated Echo in NMR Diffusion Studies. The Journal of Chemical Physics 52, 2523–2526.

Tanner JE, 1983 Intracellular diffusion of water. Archives of Biochemistry and Biophysics 224, 416–428. [PubMed: 6347071]

Tanner JE, Stejskal EO, 1968 Restricted Self-Diffusion of Protons in Colloidal Systems by PulsedGradient Spin-Echo Method. Journal of Chemical Physics 49, 1768–&.

Teh I, Zhou F-L, Hubbard Cristinacce PL, Parker GJM, Schneider JE, 2016 Biomimetic phantom for cardiac diffusion MRI. Journal of Magnetic Resonance Imaging 43, 594–600. [PubMed: 26213152]

Tofts P, 2003 Quantitative MRI of the brain : measuring changes caused by disease. Wiley, Chichester, West Sussex; Hoboken, NJ.

Tofts PS, 2004 QA: Quality Assurance, Accuracy, Precision and Phantoms Quantitative MRI of the Brain. John Wiley & Sons, Ltd, pp. 55–81.

Tofts PS, Lloyd D, Clark CA, Barker GJ, Parker GJ, McConville P, Baldock C, Pope JM, 2000 Test liquids for quantitative MRI measurements of self-diffusion coefficient in vivo. Magn Reson Med 43, 368–374. [PubMed: 10725879]

Torquato S, Jiao Y, 2010 Robust algorithm to generate a diverse class of dense disordered and ordered sphere packings via linear programming. Physical Review E 82, 061302.

Tournier JD, Yeh CH, Calamante F, Cho KH, Connelly A, Lin CP, 2008 Resolving crossing fibres using constrained spherical deconvolution: validation using diffusion-weighted imaging phantom data. NeuroImage 42, 617–625. [PubMed: 18583153]

Trudeau JD, Dixon WT, Hawkins J, 1995 The Effect of Inhomogeneous Sample Susceptibility on Measured Diffusion Anisotropy Using NMR Imaging. Journal of Magnetic Resonance, Series B 108, 22–30. [PubMed: 7627433]

van Zijl PCM, Lam WW, Xu J, Knutsson L, Stanisz GJ, 2018 Magnetization Transfer Contrast and Chemical Exchange Saturation Transfer MRI. Features and analysis of the field-dependent saturation spectrum. NeuroImage 168, 222–241. [PubMed: 28435103]

von dem Hagen Elisabeth AH, Henkelman RM, 2002 Orientational diffusion reflects fiber structure within a voxel. Magn Reson Med 48, 454–459. [PubMed: 12210909]

Wagner F, Laun FB, Kuder TA, Mlynarska A, Maier F, Faust J, Demberg K, Lindemann L, Rivkin B, Nagel AM, Ladd ME, Maier-Hein K, Bickelhaupt S, Bach M, 2017 Temperature and concentration calibration of aqueous polyvinylpyrrolidone (PVP) solutions for isotropic diffusion MRI phantoms. PLOS ONE 12, e0179276. [PubMed: 28628638]

Wang X, Reeder SB, Hernando D, 2017 An acetone-based phantom for quantitative diffusion MRI. Journal of Magnetic Resonance Imaging 46, 1683–1692. [PubMed: 28432796]

Wansapura JP, Holland SK, Dunn RS, Ball WS, 1999 NMR relaxation times in the human brain at 3.0 tesla. Journal of Magnetic Resonance Imaging 9, 531–538. [PubMed: 10232510]

Wapler MC, Leupold J, Dragonu I, von Elverfeld D, Zaitsev M, Wallrabe U, 2014 Magnetic properties of materials for MR engineering, micro-MR and beyond. Journal of Magnetic Resonance 242, 233–242. [PubMed: 24705364]

Weisskoff R, Zuo C, Boxerman J, Rosen B, 1994 Microscopic susceptibility variation and transverse relaxation: Theory and experiment. Magnetic Resonance in Medicine 31, 601–610. [PubMed: 8057812]

West KL, Kelm ND, Carson RP, Alexander DC, Gochberg DF, Does MD, 2018 Experimental studies of g-ratio MRI in ex vivo mouse brain. NeuroImage 167, 366–371. [PubMed: 29208572]

Woessner DE, 1961 Effects of Diffusion in Nuclear Magnetic Resonance Spin-Echo Experiments. The Journal of Chemical Physics 34, 2057–2061.

Xing H, Lin F, Wu Q, Gong Q, 2013 Investigation of different boundary treatment methods in Monte-Carlo simulations of diffusion NMR. Magn Reson Med 70, 1167–1172. [PubMed: 23169149]

Xu T, Foxley S, Kleinnijenhuis M, Chen WC, Miller KL, 2018 The effect of realistic geometries on the susceptibility-weighted MR signal in white matter. Magn Reson Med 79, 489–500. [PubMed: 28394030]

Yablonskiy DA, Haacke EM, 1994 Theory of NMR signal behavior in magnetically inhomogeneous tissues: The static dephasing regime. Magnetic Resonance in Medicine 32, 749–763. [PubMed: 7869897]

Yanasak N, Allison J, 2006 Use of capillaries in the construction of an MRI phantom for the assessment of diffusion tensor imaging: demonstration of performance. Magn Reson Imaging 24, 1349–1361. [PubMed: 17145407]

Yanasak NE, Allison JD, Hu TCC, Zhao Q, 2009 The use of novel gradient directions with DTI to synthesize data with complicated diffusion behavior. Medical Physics 36, 1875–1885. [PubMed: 19544807]

Yeh CH, Schmitt B, Le Bihan D, Li-Schlittgen JR, Lin CP, Poupon C, 2013 Diffusion microscopist simulator: a general Monte Carlo simulation system for diffusion magnetic resonance imaging. PLOS ONE 8, e76626. [PubMed: 24130783]

Yeung HN, Swanson SD, 1992 Transient decay of longitudinal magnetization in heterogeneous spin systems under selective saturation. Journal of Magnetic Resonance (1969) 99, 466–479.

Yuan Y, Lee TR, 2013 Contact Angle and Wetting Properties In: Bracco G, Holst B (Eds.), Surface Science Techniques. Springer Berlin Heidelberg, Berlin, Heidelberg, pp. 3–34.

Zaiss M, Schmitt B, Bachert P, 2011 Quantitative separation of CEST effect from magnetization transfer and spillover effects by Lorentzian-line-fit analysis of z-spectra. J Magn Reson 211, 149–155. [PubMed: 21641247]

Zhang H, 2016 Numerical Phantoms. Weekend Educational Course: Validation of Structural Measurements with Diffusion MRI, Proceedings of the 24th Annual Meeting of ISMRM, Singapore.

Zheng G, Price WS, 2007 Suppression of background gradients in (B0 gradient-based) NMR diffusion experiments. Concepts in Magnetic Resonance Part A 30A, 261–277.

Zhong J, Kennan RP, Gore JC, 1991 Effects of susceptibility variations on NMR measurements of diffusion. Journal of Magnetic Resonance 95, 267–280.

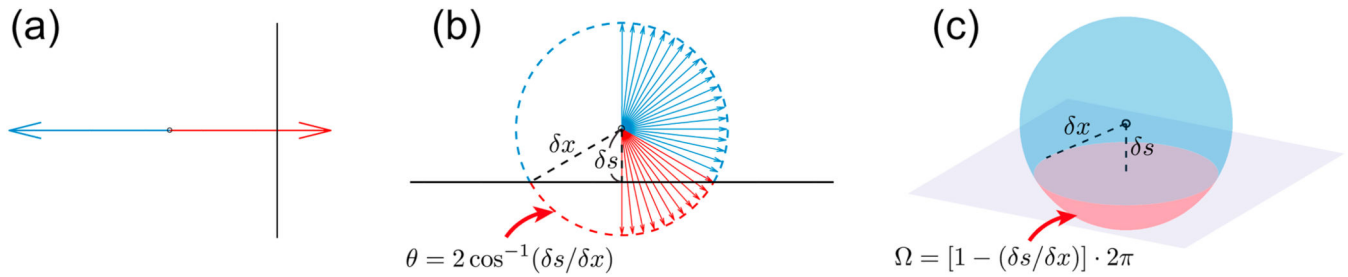

Figure 1:

Liquids that are popular test phantoms in dMRI, according to increasing complexity: a) D as a function of temperature for water, whereby ice-water is often used in multi-center studies; b) Alkanes have a relative low D compared to water (shown for dodecane and n-tridecane in right figure), but exhibit chemical shifts and ghosts when used as test liquid with EPI; c) Aqueous solutions (listed in Table 1) offer the possibility of creating a range of D-values, illustrated here for sucrose and PVP-solutions, as well as for mixtures of H_2O/acetone and D_2O/acetone (adapted from (Wang et al., 2017)); d) dairy cream (after heating) has D and K values comparable to white matter, whereby the chemical shift is used here to visualize the fat and water separately (adapted from (Fieremans et al., 2012b)); e) Liquid crystals can be prepared with microscopic μFA close to 1 (adapted from (Nilsson et al., 2018)). Adapted with permission from Wiley.

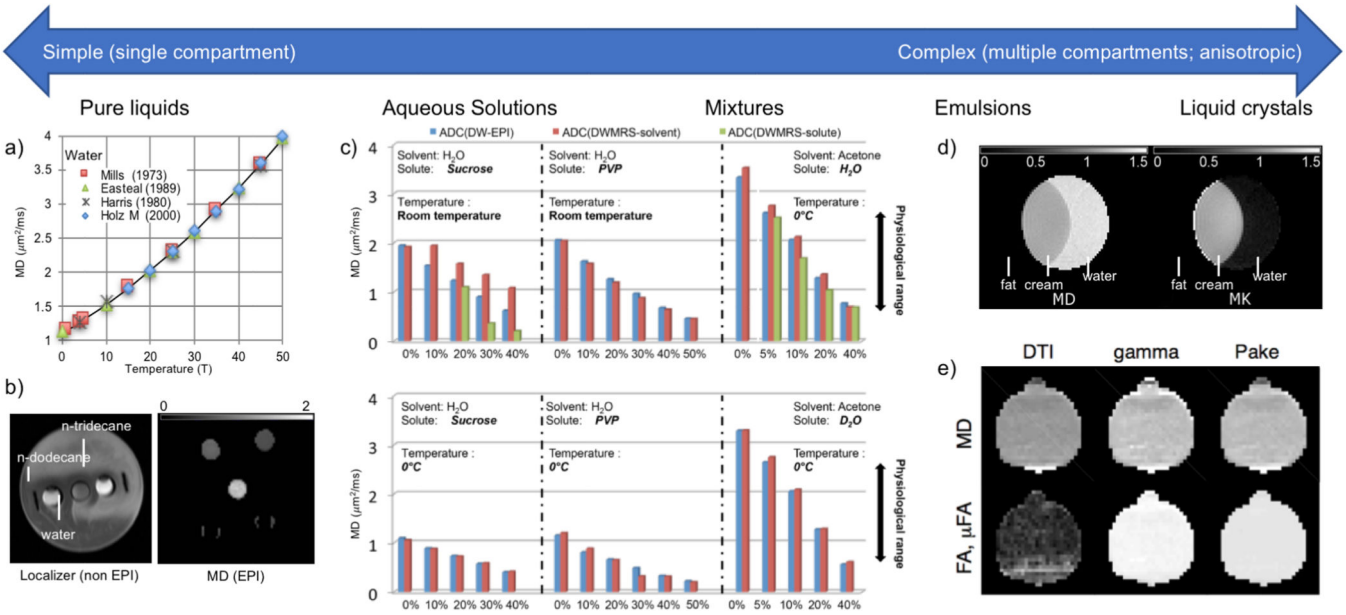

Figure 2:

Microstructural phantoms (right) mimicking brain white matter microstructure (left, SEM image of mouse brain genu of corpus callosum): the intra-axonal space (a) is modeled by glass capillary arrays (b, left, confocal transmission image adapted from (Komlosh et al., 2011)), or capillaries (b, right, electron micrograph, adapted from (von dem Hagen Elisabeth and Henkelman, 2002)); the extra-axonal space (c) is modeled by plain fiber phantoms (d, photograph and SEM image adapted from (Fieremans et al., 2008b)); both intra-, and extra-axonal space (e) is modeled by hollow fiber phantoms (f, SEM image adapted from (Guise et al., 2016)). Scale bars are added to illustrate the sizes of each phantom, as compared to the axonal microstructure. Adapted with permission from Elsevier, Wiley, and American Chemical Society.

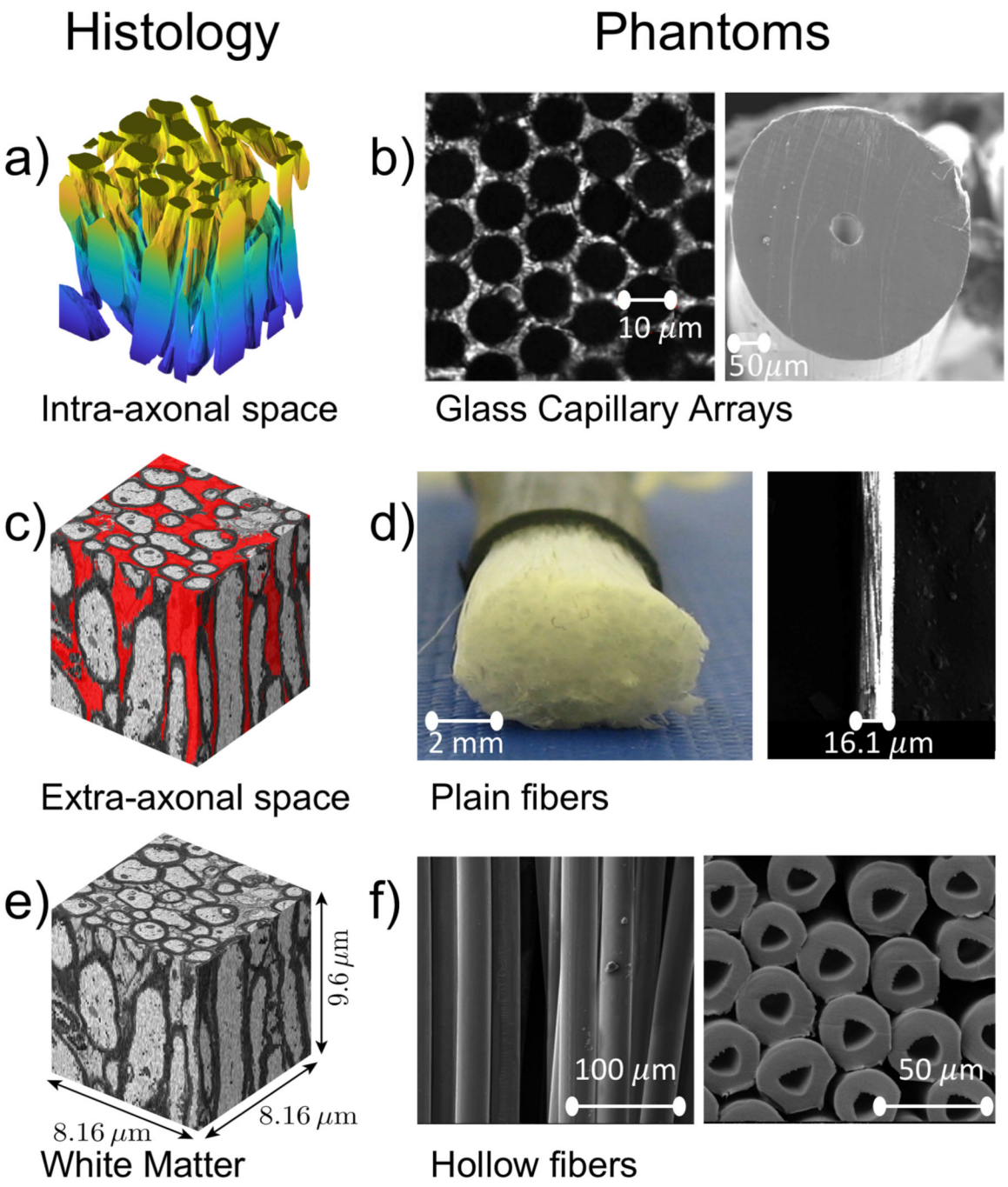

Figure 3:

The use of asparagus as a dMRI phantom (Fieremans, 2008): a) a microscopic image of a cross-section through the asparagus. The vascular bundles are indicated with ellipses; b) Close-up of the vascular bundle. Cells with a larger diameter for the xylem, which are in fact long tubular vessels with a thick wall, causing the anisotropy as measured with dMRI. The smaller cells form the phloem, which are either tubular and filled with air, or spherical and containing water; c) Resulting dMRI parametric maps; and d) fiber tracking using the asparagus as a test object for dMRI.

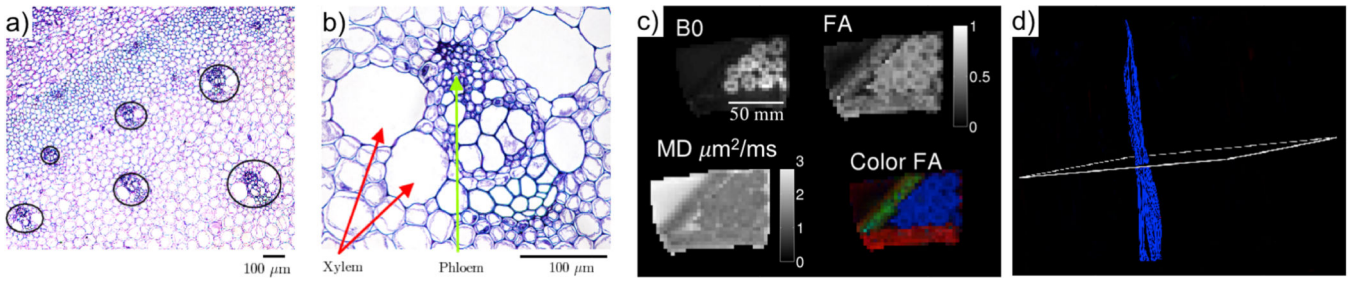

Figure 4:

Checklist illustrating the different criteria that can be used to proof check a Monte Carlo simulation framework, as explained in more details in Section 3.3. The packing geometry shown on the top right consists of 492 non-overlapping circles, and is generated by the collision-driven packing algorithm (Donev et al., 2005; Skoge et al., 2006; Torquato and Jiao, 2010); the corresponding lookup table is a 500 by 500 matrix with pixels containing no circle (black pixels), one circle (colorful pixels) and ≥ 2 circles (white pixels). In point 5 (right bottom), the left panel is a snapshot of particle densities with respect to cylinder radii at = 90 ms, explaining how to calculate the permeability (arrowhead of the right panel) based on Eq. (10) ($D_0^- = 0.2$ μm^2/ms, K = 0.05 μm/ms) and also verifying the dimensionality factor uv (Eq. (4)) in 2*d*.

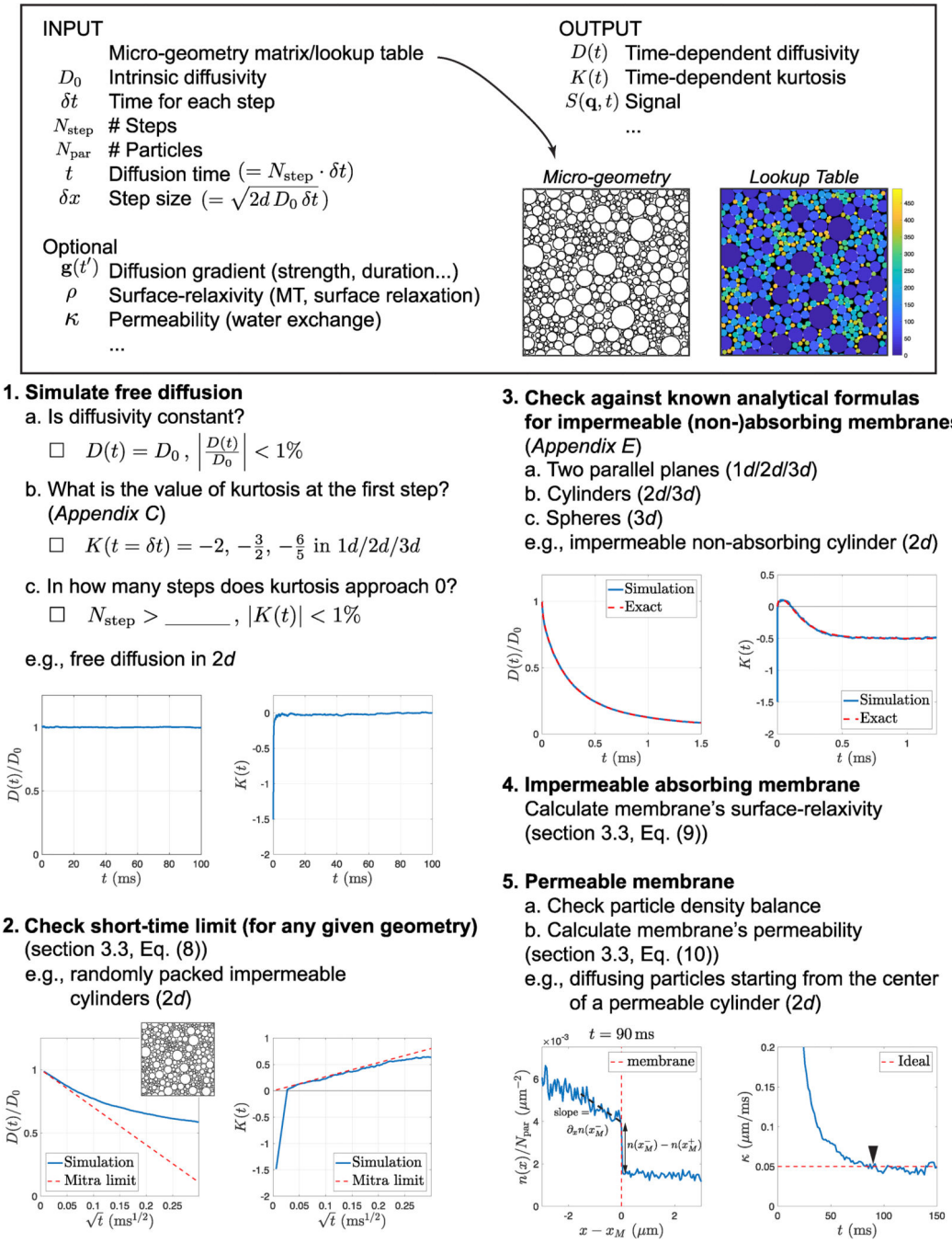

Figure 5:

Overview of numerical simulations, categorized into four quadrants, based on dimensionality (2*d* vs 3*d*), and complexity of geometry (simple shapes vs realistic microstructure). While simulations in geometries consisting of simple shapes are commonly done, our literature search revealed only few simulations in realistic neuronal microstructures performed in 2*d*, and none found so far in 3*d*. Figure adapted from (Baete et al., 2008; Chin et al., 2002; Fieremans et al., 2010; Harkins and Does, 2016; Li et al., 2014b;

Lin et al., 2016; Nguyen et al., 2014; Palombo et al., 2017; Panagiotaki et al., 2010; Xu et al., 2018) with permission from Elsevier, Wiley, IOP publishing, and Springer.

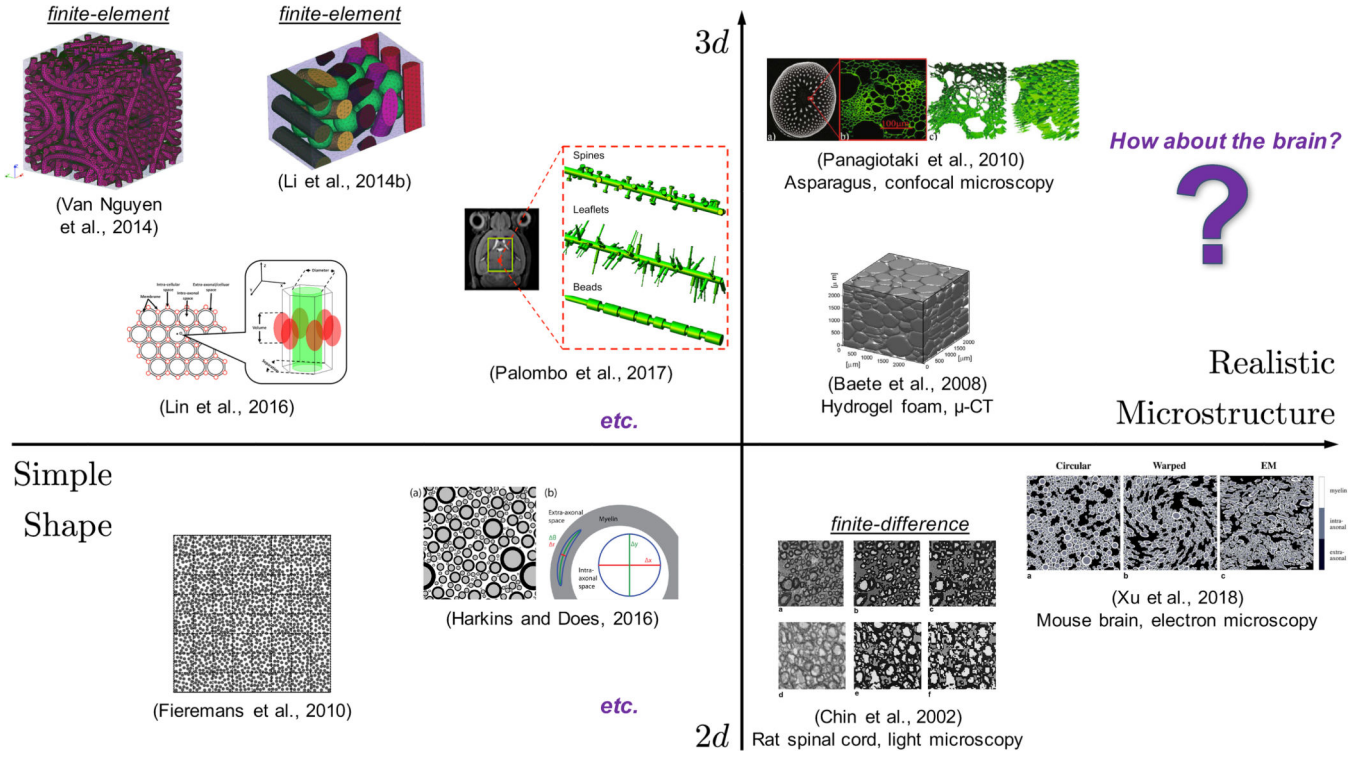

Figure A1:

The solid angle to calculate the fraction of particles (within a distance from the membrane $\delta s \lesssim \delta x$) encountering the membrane in (a) $1d$, (b) $2d$, and (c) $3d$ cases.

Table 1:
Liquid phantoms proposed for diffusion 1 MRI of the brain

Overview of liquid phantoms proposed for diffusion MRI, listing their diffusion properties, potential advantages and disadvantages, and corresponding references. Diffusion coefficients D are given at room temperature unless temperature is stated. Corresponding examples are also shown in Figure 2

Phantom	Diffusion properties	Advantages	Disadvantages	References
Water Ice Water	D=2.0 μm^2/ms (20°C) D=1.1 μm^2/ms (0°C)	Inert, readily available Temperature-controlled Long T_1 and T_2, hence often used to combine with hollow/plain fibers in phantoms (Table 2)	D higher than brain; Low viscosity Ice water: Preparation needed for every use	(Chenevert et al., 2011; Malyarenko et al., 2016; Mulkern et al., 2015)
decamethylcyclopentasiloxane (C10H30O5Si5)	D=0.16 μm^2/ms	Stable, single peak in proton NMR spectrum, suitable for gradient calibration Used in glass capillary array phantoms (Table 2)	Different chemical shift than water protons	(Komlosh et al., 2017; Wagner et al., 2017)
Alkanes (N- and cyclic)	D=0.5 – 1.4 μm^2/ms	Range of D-values	Flammable, multiple spectral lines (linear)	(Dowell and Tofts, 2010; Tofts, 2004; Tofts et al.,2000)
Ethylene glycol	D=0.071 μm^2/ms	Used as thermometer, suitable for gradient calibration	Toxic, should be handled with care	(Spees et al., 2012)
Sucrose solutions	D= 0.5 – 1.4 μm^2/ms	Range of D-values	Multiple spectral lines Not Gaussian diffusion	(Delakis et al., 2004; Hara et al., 2014; Laubach et al., 1998; Lavdas et al., 2013; Wang et al., 2017)
PVP solutions	D= 0.3 – 1.6 μm^2/ms	Range of D-values	Challenging to prepare high concentration solutions	(Pierpaoli et al., 2008; Wagner et al., 2017; Wang et al., 2017)
Acetone/ deuterium oxide mixture	D= 0.5 – 3 μm^2/ms (0°C)	Range of D-values	Limited shelflife, costly, flammable	(Wang et al., 2017)
Cream (after heating)	D=1.1 μm^2/ms K=1.1	Fat-water shift enables independent prediction of D and K	Preparation needed for every use	(Fieremans et al., 2012b)
Liquid crystals	D= 0.37 μm^2/ms μFA ≈ 1	Well-characterized microscopic anisotropy	Preparation needed Temperature sensitive	(Nilsson et al., 2018)

Neuroimage. Author manuscript; available in PMC 2019 November 15.

Table 2:

Anisotropic phantoms proposed for diffusion MRI of the brain

Overview of anisotropic phantoms proposed for diffusion MRI, listing the relevant sizes in [μm] and materials, potential application, and corresponding references. Corresponding examples are shown in Figure 2 and Figure 3.

Phantom	Sizes [μm]	Material	Applications	References
Capillaries	23, 48, 82	Glass (Schott North America, Southbridge, MA, USA)	DTI phantom	(Yanasak and Allison, 2006; Yanasak et al., 2009)
Capillary wafers or glass capillary array (GCA)	2.5, 10, 15, 13.7 (only I.D.)	Glass (Photonis, Sturbridge, MA, USA)	Modeling restricted diffusion, pore size mapping with dPFG	(Benjamini et al., 2014; Komlosh et al., 2011)
Capillaries	I.D.: 1 – 50 O.D.: 75, 150	Fused Silica (Polymicro Technologies – Molex)	Modeling restricted diffusion, diameter mapping, crossing fibers	(Avram et al., 2004; Bar-Shir et al., 2008; Li et al., 2014a; Milne and Conradi, 2009; Morozov et al., 2013, 2015; Shemesh et al., 2010; Siow et al., 2012; Tournier et al., 2008)
Capillary sheets	I.D: 50 O.D.: 350	Plastic (PTFE) (Cole-Parmer Instrument)	Crossing fibers	(Lin et al., 2003; von dem Hagen Elisabeth and Henkelman, 2002)
Hollow fibers	I.D: 11.8 ± 1.2 O.D.: 33.5 ± 2.3	Polypropylene	Characterization, fiber tracking, diameter mapping	(Fan et al., 2018; Guise et al., 2016)
Hollow fibers (taxons)	I.D.: 9.5 – 13.4	Co-electric spun fibers	Characterization	(Hubbard et al., 2015)
Plain fibers	O.D.: 17	rayon	Crossing fibers	Perrin M. *et al.* Philos Trans R Soc Lond B Biol Sci 2005
Plain fibers	O.D.: 17	Dyneema® polyethylene	Characterization, biophysical modeling of $D(t)$, QA, effect of susceptibility and surface relaxation on diffusion	(Burcaw et al., 2015; Farrher et al., 2012; Fieremans et al., 2008a; Fieremans et al., 2008b; Lemberskiy et al., 2017; Lorenz et al., 2008; Reischauer et al., 2009)
Plain fibers	O.D.: 20	Acrylic	Crossing fibers	(Poupon et al., 2008)
Plain fibers	O.D.: 15	Polyamide	Modeling effect of susceptibility on diffusion	(Laun et al., 2009)
Plain fibers	O.D.: 10	Polyester	Crossing fibers	(Pullens et al., 2010)
Plants	~ 100	Asparagus, Celery	Sequence testing, Modeling of susceptibility	(Baete et al., 2013; Boujraf et al., 2001; Lätt et al., 2007; Panagiotaki et al., 2010; Sigmund and Song, 2006)